University of Nebraska - Lincoln
DigitalCommons@University of Nebraska - Lincoln

Engineering Mechanics Dissertations & Theses

Mechanical & Materials Engineering, Department of

Spring 5-2010

MECHANICAL MILLING OF CO-RICH MELT-SPUN SM-CO ALLOYS

Farhad Reza Golkar-Fard
University of Nebraska - Lincoln, farhad518@huskers.unl.edu

Follow this and additional works at: https://digitalcommons.unl.edu/engmechdiss

 Part of the Engineering Mechanics Commons, and the Mechanical Engineering Commons

Golkar-Fard, Farhad Reza, "MECHANICAL MILLING OF CO-RICH MELT-SPUN SM-CO ALLOYS" (2010). *Engineering Mechanics Dissertations & Theses*. 6.
https://digitalcommons.unl.edu/engmechdiss/6

This Article is brought to you for free and open access by the Mechanical & Materials Engineering, Department of at DigitalCommons@University of Nebraska - Lincoln. It has been accepted for inclusion in Engineering Mechanics Dissertations & Theses by an authorized administrator of DigitalCommons@University of Nebraska - Lincoln.

MECHANICAL MILLING OF CO-RICH MELT-SPUN SM-CO ALLOYS

by

FARHAD REZA GOLKAR-FARD

A THESIS

Presented to the Faculty of

The Graduate College at the University of Nebraska

In Partial Fulfillment of Requirements

For the Degree of Master Science

Major: Engineering Mechanics

Under the Supervision of Professor Jeffrey E. Shield

Lincoln, Nebraska

May, 2010

MECHANICAL MILLING OF CO-RICH MELT-SPUN SM-CO ALLOYS

Farhad Reza Golkar-Fard, M.S

UNIVERSITY OF NEBRASKA, 2010

Advisor: Jeffrey E. Shield

Rare-earth, high-energy permanent magnets are currently the best performing permanent magnets used today. The discovery of single domain magnetism in 1950's ultimately led to the development of nanocomposite magnets which had superior magnetic properties. Previous work has shown that mechanical milling (MM) effectively generates nanoscale structures in Sm-Co-based alloys. MM of more Co-rich, melt-spun Sm-Co alloys (up to the eutectic composition) and the role of initial structure on the milling behavior were investigated.

Sm-Co alloys with compositions of $Sm_{10.5}Co_{89.5}$ and Sm_8Co_{92} were produced by arc melting, melt-spinning and mechanical milling. X-ray diffraction results showed that the as-melt spun materials formed in the disordered $TbCu_7$-type variant for both compositions, and that FCC-Co is also present in Sm_8Co_{92}. At long milling times, FCC-Co developed in the $Sm_{10.5}Co_{89.5}$ alloy. MM resulted in a decrease of grain size, indicated by the broadening of the x-ray diffraction peaks. However, the samples remained crystalline, as peaks characteristic of the $TbCu_7$-type structure were always present. The grain sizes obtained in both compositions ranged between 10-20 nm. Scanning electron microscopy images showed that the powder particles contain agglomerates and that a broad micron-scale particle size exists in the samples. The coercivity of both samples

initially increased with increasing milling time, reaching plateau values of ~4.6 kOe and 1.6 kOe for $Sm_{10.5}Co_{89.5}$ and Sm_8Co_{92}, respectively. The lower coercivity values of the Sm_8Co_{92} alloy were due to its more Co-rich composition.

Acknowledgment

Many people have been involved in my thesis work and contributed not only with their presence and kindness but also with their knowledge and competence.

I would like to start by first giving my deepest gratitude to my advisor, Dr. Jeffrey E. Shield. His guidance, advice, and commitment have not only made me progress in my research but also inspired me to continue my academic endeavors.

I would like to give special thanks to Dr. Mehrdad Negahban from University of Nebraska, Dr. Lennart Wallström and Dr. Janis Varna from Lulea University of Technology in Sweden. I am grateful to them for giving me the opportunity to study in the EMME program. I would also like to thank the ATLANTIS program and Office of Naval Research (under grant no. N00014-09-1-0620) for their funding of the EMME program and the project, respectively.

I would like to thank all members of my research group: Paul, Wendy, Jay, Jeremy, Eldon, and of course the coffee machine. I am thankful for all their help, for sharing their knowledge, and for always having time for chitchat. I would also like to thank all my other friends, especially Jiri and James, for their support and understanding.

Most importantly, I would like to give my deepest gratitude to my family for their love, wisdom, and endless encouragement throughout my entire life. Finally, I would like to dedicate this work to my niece, Emilie Golkar, whom I truly love and miss so much.

Abstract

Table of Contents

List of Figures

List of Tables

Chapter 1. Introduction

1.1 Significance of the study

Permanent magnets have become a vital component in a wide range of industrial, consumer and defense applications (1). The growth of permanent magnet production has been substantial over the past century: approximately 12,000 tons of permanent magnets (valued at US $100 million) in 1955 increased to estimated 180,000 tons (valued at US $1 billion) in 1985 (1; 2). Today, the total world production of permanent magnets is estimated to be 250,000 tons per year with an annual growth rate between 10 % and 20 % (3). The largest producers of permanent magnets are located in Japan and China, followed by USA and Europe (3).

The introduction of Alnico to the market in the 1930's showed to have superior magnetic properties compared to available magnets at that time (2). In 1970's and 80's the magnetic properties improved nearly tenfold with the introduction of Sm-Co and Nd-Fe-B alloys. Sm-Co and Nd-Fe-B later came to be known as rare-earth high-energy permanent magnets and are characterized by their superior magnetic properties (2).

Discovering new magnetic phases which can match the rare-earth permanent magnets has proven to be very difficult and thus efforts are being made on improving existing rare-earth permanent magnets. One breakthrough in improving existing magnets came in the 1950's with the discovery of single domain magnetism which led to research in nanophase hard magnetic materials and nanocomposite magnets (4). Nanocomposite

magnets consist of a mixture of exchange-coupled magnetically soft and hard nanograins and have resulted in higher energy products than conventional magnets (4).

Techniques such as melt-spinning and mechanical milling have shown to be successful in the development of nanocomposite magnets. The melt-spin uses a process where the sample is melted and rapidly solidified, producing nano-crystalline grain structures. Hadjipanayis (4) reported in the 1980's a breakthrough that occurred in the nanocomposite research: researchers were able to obtain large coercivity on nanosized melt-spun Nd-Fe-B and Pr-Fe-B(Si) alloys. This discovery led to other alloys, such as Sm-Co, being made with the melt-spinning technique and resulting in nanoscale microstructure and large values of coercivity (4).

Mechanical milling is the other common technique used to develop fine-grained particles of intermetallic compounds. In mechanical milling, the sample and milling balls are placed inside a sealed vial and shaken. Impact energy at the moment of collision between the balls, powder and the wall of the vial, leads to fracture and welding of the sample particles (5). Mechanical milling was first shown to be successful on Nd-Fe-B alloys and later it was applied to other hard magnetic alloy systems such as Sm-Co (6). An extensive study on Sm-Co based alloy showed that mechanical milling refine the as-milled powder grains resulting in enhancement of the magnetic property (7; 6; 8).

The commercial success of a permanent magnet material is a function of the cost, availability and geographic source of its elements (1 p. 10). Sm is a rare and expensive element. For lowering the cost of producing Sm-Co based magnets, extensive studies are

undertaken in the Co-rich region of Sm-Co alloy. The aim has been to try partly replacing Sm without the magnet losing its superior magnetic properties (3; 6; 9; 10).

1.2 Objectives

The objective of this study was to produce Co-rich Sm-Co alloys to minimize the use of the rare earth elements and to develop two-phase nanocomposite materials that have superior magnetic properties. An investigation of the role of mechanical milling of more Co-rich alloys (up to eutectic compositions) and the role of initial structure on the milling behavior was conducted.

Chapter 2. Literature Review

2.1 A brief history of magnetism

The history of magnetism goes back as far as around three thousand years and can be divided into seven "ages" (2). The time span of the ages, significant discoveries, magnetic material used, and the applications/devices for the different ages are outlined in Table 1. In ancient and early ages, iron and lodestones were the main materials used in the magnetic applications, such as compasses and horseshoe magnets. Afterwards came the electromagnetic age which features Oersted's accidental discovery of the relationship between electricity and magnetism in 1820 and steel being the main magnetic material used in the applications (2). The discovery led to development of applications such as the telegraph, generators, and motors (2). Then came the age of understanding and the introduction of Al-Ni-Co alloy (Alnico). Alnico showed to have superior magnetic properties compared to available magnets at that time (2). The age of understanding marked the intellectual summit in the history of magnetism followed by ages where most of the people on earth could start benefiting from the magnetic technologies such as television, radar, and magnetic resonance imaging (MRI) (2). Approximately 30 years later Sm-Co alloy was introduced to the market with better intrinsic magnet properties than Alnico (9). Then in the 1980's, due to problems with supply of cobalt, Nd-Fe-B alloys with similar magnetic properties to Sm-Co alloys were discovered (11 p. 317). Sm-Co and Nd-Fe-B came to be known as *rare-earth magnets* and was characterized by their superior magnetic properties (2). Rare-earth magnets are used frequently in applications such as electrical motors, generators, and loudspeakers (2; 11 p. 79).

Table 1. ***The seven ages of magnetism*** **(2)**

Age	Time	Materials	Applications/devices
Ancient	~1000 BC- 1500 AD	Iron, Lodestone	South-pointer, compass
Early	1500-1820	Iron, Lodestone	Dip circle, Horseshoe magnet
Electromagnetic	1820-1900	Electrical steels	Motors, generators, telegraph
Understanding	1900-1935	Al-Ni-Co	
High Frequency	1935-1960	Ferrites	Radar, television, MRI
Applications	1960-1995	Nd-Fe-B & Sm-Co	Consumer electronics
Spin electronics	1995 -	Multilayers	High density magnetic recording

2.2 Basic Concepts

Unit system

The magnetic properties can either be expressed in SI-unit [meter-kilo-second] or cgs-emu [centimeter-gram-second-electromagnetic]. The units for both systems, as well as the conversion factors, are presented in Table 2. In this thesis, the cgs-emu system will be used.

Definitions

Oersted's discovery in 1820 proved to be of great value for the development in the field of magnetism. He discovered that a magnetic field *H* [Oe] is produced whenever there is an electrical charge in motion (11 p. 1). However, a magnetic field can also be produced in the absence of an electric current. This is the case for a permanent magnet, where the orbital and spin motion of electrons produces the magnetization within the material and creates a magnetic field outside (11 p. 1).

When a magnetic field is applied to a material, the material will respond with a magnetic induction or magnetic flux density. The induction or flux *B* [G] is a vector quantity and is related to the magnetic field by

$$\boldsymbol{B} = \mu \boldsymbol{H} \qquad \text{(Eq. 1)}$$

where μ is the permeability of the medium (12 pp. W21-23). The permeability of a material is a measure of the degree to which the material can be magnetized, i.e. a

material with high permeability can concentrate a large amount of flux density in its interior (13 pp. 11-17).

Another important vector quantity is the magnetization *M* which is defined as the magnetic moment per volume [emu/cm^3] and is proportional to the applied field as follow

$$\boldsymbol{M} = \chi_m \boldsymbol{H} \qquad \text{(Eq. 2)}$$

where χ_m [dimensionless] is the magnetic susceptibility. The susceptibility is often used to classify materials since it indicates how responsive a material is to an external magnetic field (13 p. 13). Further, the magnetization is related to the magnetic field and magnetic induction as followed (13 pp. 11-17)

$$\boldsymbol{B} = \boldsymbol{H} + 4\pi\boldsymbol{M} \qquad \text{(Eq. 3)}$$

Table 2. ***Magnetic units and conversion factors for the SI and cgs-emu system*** **(12 pp. W21-23; 13 pp. 11-17).**

Quantity	Symbol	SI-unit	Cgs-emu unit	Conversion factor
Magnetic induction	B	Tesla [T]	Gauss [G]	1 G= 10^{-4} T
Magnetic field strength	H	Ampere/m [A/m]	Oersted [Oe]	1 Oe= 79.58 A/m
Magnetic moment	m	Ampere m^2[A m^2]	emu	
Magnetization	M	Weber/m^2 [Wb/m^2]	emu/cm^3	1 emu/cm^3= 12.57×10^{-4} Wb/m^2
Permeability	μ	Henry/m [H/m]	Gauss/Oersted [G/Oe]	1 G/Oe = 1.257×10^{-6}H/m

Origins of magnetic moments

At the absence of an external magnetic field, the magnetic moments of a free atom consist of contributions from orbital and spin motions of electrons (11 p. 1). In the *orbital* motion the electron is moving around the nucleus generating a very small magnetic field and a magnetic moment along the axis of the orbital rotation (12 pp. W23-24). The second magnetic moment contribution is the *spin* motion where the electron spins around its own axis generating moment along its axis (12 pp. W23-24). The direction of the magnetic moment, for both cases, will be either up or down depending on the direction of their respective motion (right hand rule applies). These two magnetic moments will interact with each other and the resulting interaction is called the *spin-orbit coupling* (13 p. 27). The magnitude of this coupling is determined by the charge on the atomic nucleus, which in turn depends on the atomic number (13 p. 28). In Figure 1, the magnetic moment associated with orbital and spin motion are schematically illustrated.

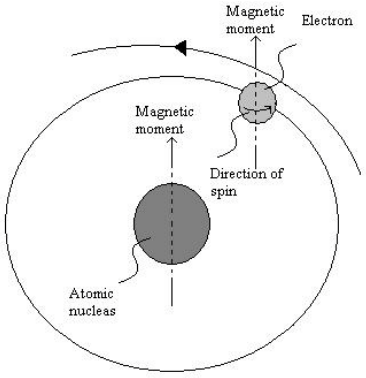

Figure 1. Schematic illustration of magnetic moment associated with an orbiting electron and spinning electron.

Further, the net magnetic moment of an atom is the summation of the magnetic momentum of each individual orbital motion and spin motion. However, the Pauli exclusion principle states that each atomic orbital may only be occupied by a maximum

of two electrons and the electrons in the same atomic orbital must have opposite spin (13 p. 27). This leads to a total cancellation of both orbital and spin moment for materials composed of atoms having completely filled electron shells (12 p. W24). Atoms of rare-earth and transition elements have unfilled f-orbital and d-orbital, respectively, making it possible for them to be permanently magnetic (14 p. 6).

2.3 Types of magnetic materials

Copper, gold and silver are some examples of *diamagnetic* materials which are characterized by being non-permanent and have magnetic field response that exists only when an external magnetic field is applied (11 p. 33). When an external magnetic field is applied to the diamagnetic material, the orbital motion of the electrons will change direction resulting in the magnetic moment being opposite to the applied field which is schematically illustrated in Figure 2 (13 p. 34).

In *paramagnetic* materials, the atomic magnetic dipoles are randomly oriented in the demagnetized state. The effects of these dipoles cancels out and results in a zero net magnetic moment (12 p. W25). But contradictory to the diamagnetic materials, when an external magnetic field is applied, the atomic dipoles of paramagnetic material will align in the same direction as the applied external field, see Figure 2 (12 p. W25). Examples of paramagnetic materials are titanium, aluminum, and magnesium (12 p. W26).

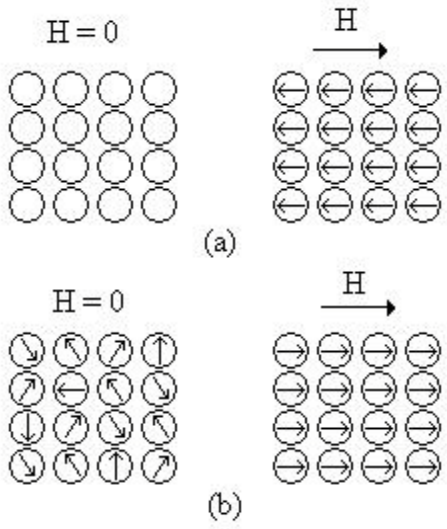

Figure 2. The atomic dipole configuration with and without an external field for (a) diamagnetic material and (b) paramagnetic material (12 p. W25).

In *ferromagnetic* materials, small regions exist where all the magnetic dipoles inside are aligned parallel to each other, resulting in saturation magnetization inside the region (13 p. 73). These regions are called *domains* and each domain has a different magnetization direction, which result in the total magnetization averages to zero in the demagnetized state (13 p. 73). If a magnetic field is applied to the ferromagnetic material, the domains will align with the direction of the applied field and reach saturation magnetization. Even in the absence of an external field, the ferromagnetic materials possess a permanent magnetic moment and manifest very large and permanent magnetizations (12 p. W26). This permanent magnetic moment is a result of mainly un-cancelled electron spins but also a small contribution from un-cancelled orbital-spin (12 p. W26). Notably, the saturation magnetization decreases gradually with increasing temperature and then abruptly drops to zero at a specific temperature called the Curie temperature (12 p. W32).

Elements such as cobalt, nickel, and some of the rare-earth materials are considered to be ferromagnetic materials (12 p. W26).

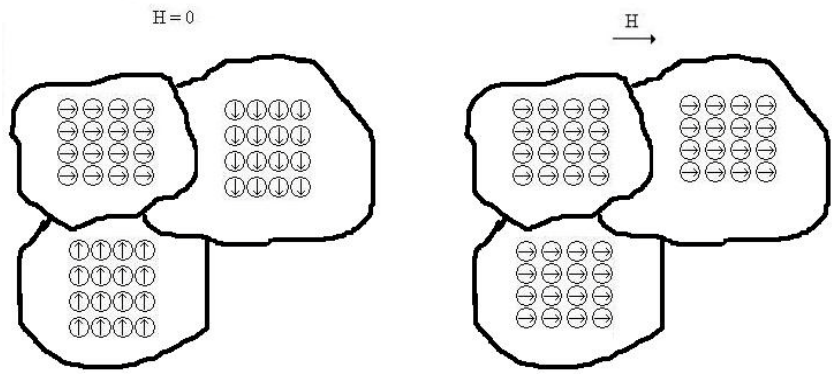

Figure 3. Schematic illustration of domains with the magnetic dipoles inside which are aligned parallel to each other. When an external field is applied, the domains tend to align with the field.

In *antiferromagnetic* materials the magnetic dipoles have same magnitude and are aligned anti-parallel to each other, see Figure 4, resulting in a zero net magnetic moment (13 p. 89). Antiferromagnetic materials respond to external magnetic fields in a similar way to the paramagnetic materials (13 p. 89). The antiferromagnetic materials become paramagnetic above a specific temperature called the Néel temperature. Examples of antiferromagnetic materials are Chromium and Manganese (11 p. 195).

The *ferrimagnets* behave very much like the ferromagnets in the way that they have a spontaneous magnetization below the Curie temperature, organized into domains, exhibit hysteresis, and saturation in their magnetization curves (11 pp. 195-196). The ferrimagnets are also related to antiferromagnets, in that their magnetic dipoles are aligned anti-parallel to each other. However, a total magnetization exists in ferrimagnets, because the magnetization of one sublattice is greater than that of the oppositely oriented

sublattice. This is schematically illustrated in Figure 4 (13 p. 107). Fe_3O_4 is an example of a ferrimagnet (11 p. 196).

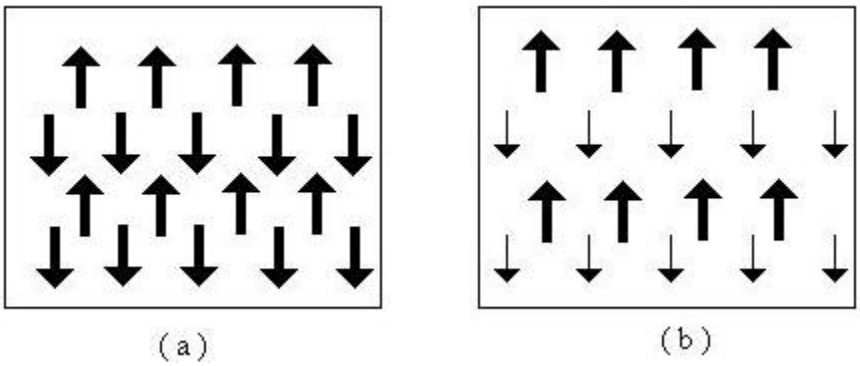

Figure 4. Schematic illustration of (a) an antiferromagnetic and (b) a ferromagnetic material.

2.4 Domains

As discussed earlier, a domain is a region, normally in the microscopic size, where the magnetic dipole moments inside the domain are aligned in the same direction. This will result in saturation magnetization inside the domain in that direction (4 pp. W33-34). For the entire solid, the magnitude and direction of the magnetization will be the vector sum of the magnetizations and directions of each individual domain.

2.4.1 Domain energy

Domains are formed in ferromagnetic materials as a result of minimization of total magnetic energy (13 p. 75). The total magnetic energy is related to several energies including exchange, magnetostatic, and magnetocrystalline energy.

The *exchange energy*, which aligns the electron spins, is minimized when all magnetic moments point in the same direction (14 p. 8). This implies that lowest exchange energy is obtained when a single domain with all magnetic moments align occurs (13 p. 75). However, the energies discussed below have larger contributions to the total energy and define domain formation (14 p. 8).

Landau and Lifschitz showed in 1935 that a single domain specimen is associated with large *magnostatic energy*. This is because the magnetostatic energy is related to the demagnetizing field of the ferromagnet (11 p. 118; 13 p. 75) .The demagnetization field will be discussed more thoroughly in chapter 2.7.3. The magnetostatic energy is believed to be the principal driving force of domain formations since breaking the magnetization into domains will reduce the demagnetizing field and thus minimize the magnetostatic energy (11 p. 118; 13 p. 75).

Within the crystal lattice, there are directions in which the magnetization prefers to lie. These directions are termed “easy” axes since it is easier to magnetize with an external magnetic field along these directions (14 p. 9). The *magnetocrystalline* energy is a measure of domain orientation with respect to crystallographic directions of the material and to minimize this energy the domains will have to form along the easy axes of the material (14 p. 9; 13 p. 76).

2.4.2 Domain walls

The direction of the magnetic dipole alignments inside the domain can vary from one domain to another and the adjacent domains are separated by a *domain wall*. Across this

distance the direction of magnetization gradually changes as Figure 5 schematically illustrates (13 p. 79). The width of the domain walls can very and is determined by a balance between the exchange energy and magnetocrystalline anisotropy (13 p. 80). The exchange energy favors adjacent magnetic moments being parallel, or as close to parallel as possible (13 p. 80). Therefore, wide walls are preferred by the exchange energy since the changes in moment angles between the moments will be small. On the other hand magnetocrysalline anisotropy favors narrow walls with a sharp transition between the domains (13 p. 80). Magnetocrystalline anisotropy is optimized when the moments are aligned as closely to the easy axes and only few moments being unfavorable crystalline aligned in the transition region (13 p. 80). The domain wall width δ_0 is determined when these two energies form a balance and can be found by using the equation

$$\delta_0 = \sqrt{\frac{A}{K_1}} \qquad \text{(Eq. 4)}$$

where A is the exchange stiffness coefficient and K_1 is the leading term in magnetocrystalline anisotropy (15 p. 123). The domain wall width can vary from about one nanometer in extremely hard materials (high K_1) to several hundred nanometers in very soft materials (15 p. 123). The domain wall width for $Nd_2Fe_{14}B$, $SmCo_5$, and Sm_2Co_{17} are approximately 5.2, 5.1, and 10.0 nm wide, respectively (11 p. 319).

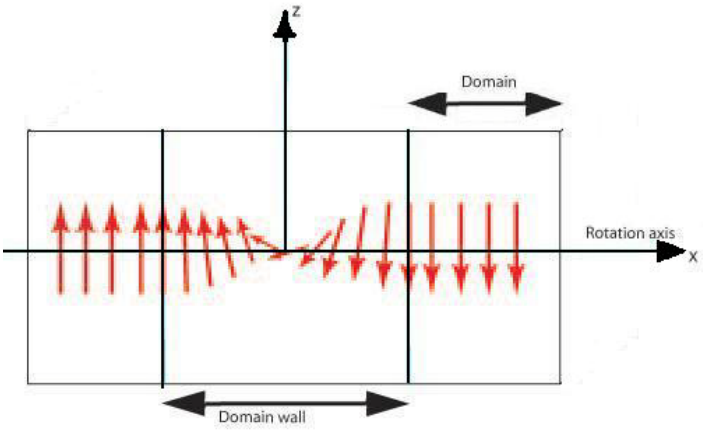

Figure 5. Schematic illustration of domains and domain wall: arrows represent the atomic magnetic dipoles. It can been seen that the change in orientation of the magnetic dipoles in a 180° twist boundary (13 p. 80; 16).

2.4.3 Domain movement due to an external field

In the initial demagnetized state, the domains are arranged such that the magnetization averages to zero (13 p. 81). Applying a low magnetic field to the sample will result in that domains which are in the same direction as the external field will start growing, due to domain wall motion, while those domains opposing the field will reduce its size. Increasing the magnetic field further will force domains unfavorably orientated to overcome their anisotropy energy and start rotating towards the direction of the applied field (11 p. 121). This growth and rotation of the dipoles will continue until all domains are oriented in the same direction as the applied field (11 p. 121). This process of domain movement with increasing magnetic field is schematically illustrated in Figure 6.

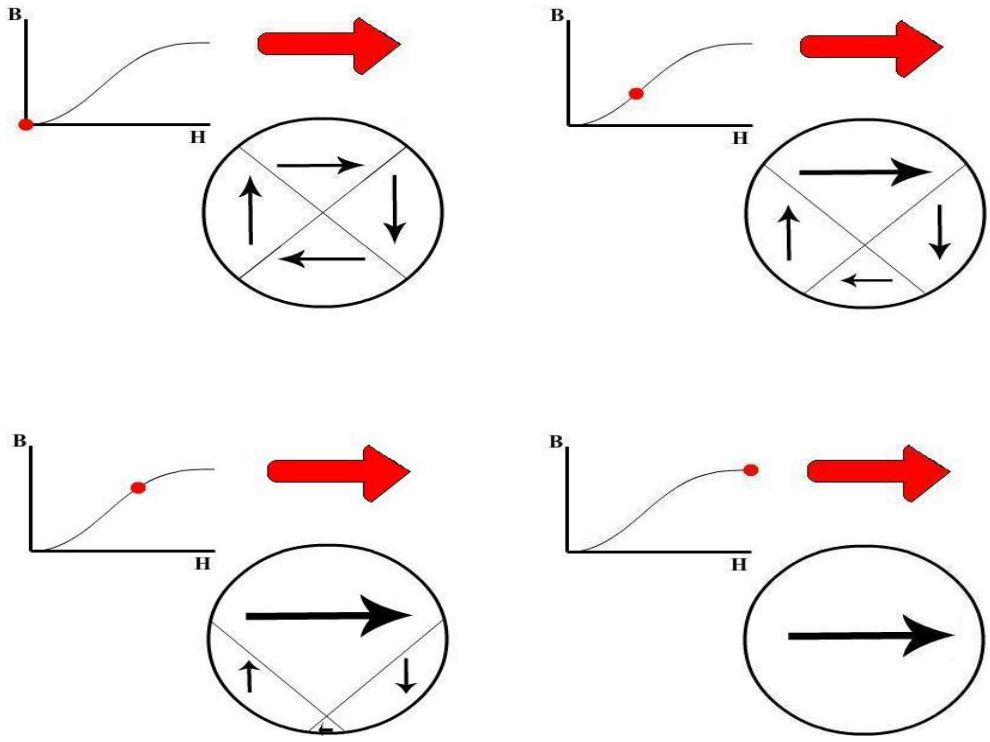

Figure 6. By following the red dot in the B-versus-H diagram, one can see that the domains (inside the circle) that has direction closest to that of applied field (big red arrow) grows at the expense of the other domains. At the final stage the domain will align with the applied field and the magnetization of the material at this stage is called the saturation magnetization (16).

2.4.4 Single domain

As discussed in chapter 2.4.1, the total magnetic energy will decrease with formation of multiple domains. However, under a certain particle radius r_c, it will be energetically unfavorable to form domain walls and instead a single-domain particle is formed (13 p. 137). For a single-domain particle the magnetostatic energy will be large but on the other hand there will be no domain wall energy while for a multi-domain particle it is the other way around (13 p. 137). Figure 7 shows the energy of single and multi-domain particles as a function of the particle radius (13 p. 137). Large single-domain particles can form if

either the domain wall energy is large so that wall formation is unfavorable, or if the saturation magnetization is small, so that the magnetostatic energy is small (13 p. 137). The critical radius can be calculated by

$$r_c = \frac{36\sqrt{AK_1}}{\mu_0 M_S^2} \qquad \text{(Eq. 5)}$$

where μ_0 is the permeability of free space and M_s is the saturation magnetization (17; 14 pp. 10-11).

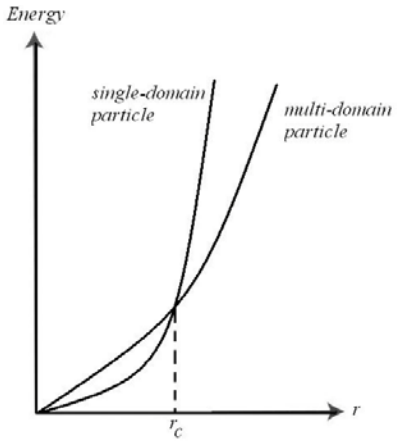

Figure 7. The energy of single and multidomain as a function of particle radius (13 p. 137).

2.5 Hysteresis

One way to represent the magnetic properties of a material is by plotting the magnetic induction or magnetization as a function of magnetic field (11 p. 70). The curve in Figure 8 is a typical *hysteresis* loop and several important magnetic properties can be interpreted from the loop.

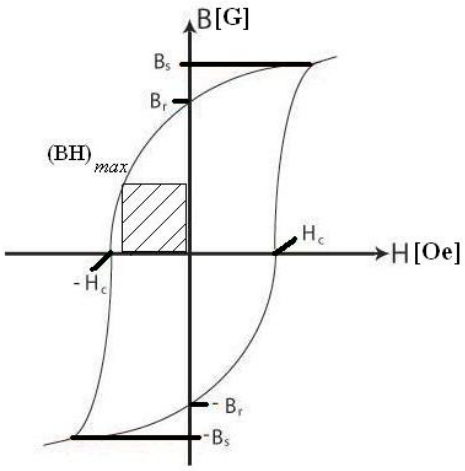

Figure 8. A typical B-H hysteresis loop (16).

With applied field **H** increasing the magnetic induction (magnetization) will start to increase non-linearly up to *saturation induction* $\boldsymbol{B}_s$ (*magnetization* $\boldsymbol{M}_s$). All the domains are, at this point, rotated and orientated in the same direction (11 p. 71). Then **H** is reduced to zero and the remaining magnetic induction is called the remanence induction $\boldsymbol{B}_r$ (remanence magnetization $\boldsymbol{M}_r$) (11 p. 72). To reduce the magnetization of the material back to zero, an **H**-field termed coercivity $\boldsymbol{H}_c$. in the opposite direction is required. If **H**-field is further increased in the opposite direction the saturation induction $-\boldsymbol{B}_s$ (magnetization $-\boldsymbol{M}_s$) will be reached again but in the opposite direction. The cycle is then reversed.

A significant property which can be calculated from the hysteresis loop is the *energy product* $\mathbf{(BH)}_{max}$. The energy product represents the magnetic energy stored in the magnet material and is obtained by calculating the largest rectangular-area under the curve inside the second quadrant. (12 p. W41). High coercivity and remanance will result in a high

energy product. The energy product is usually measured in MegaGauss-Oersted [MGOe] (11 p. 302). The conversion factor between MGOe and J/m^3 [SI-unit] are as follow

$$1\ MGOe \equiv 7.96\ kJ/m^3$$

The ferromagnetic materials can have different hysteresis loop shapes depending on their characteristics. If the magnet has low coercivity, high saturation magnetization, high remanance, and low energy product it is said to be a *soft* magnet. The hysteresis loop of a soft magnet will therefore be narrow and thin (12 p. W39). *Hard* magnets on the other hand are characterized by having high coercivity, low saturation magnetization, low remanance, and high energy product. A schematic illustration of the hysteresis loop for both soft and hard magnet is presented in Figure 9 (12 p. W41).

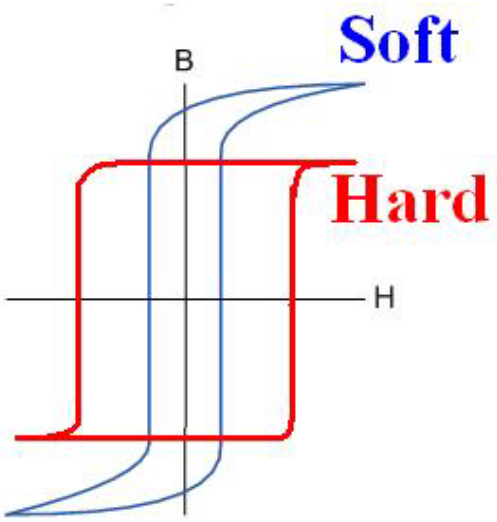

Figure 9. Typical hysteresis loop for soft and hard magnet (12 p. W39).

2.6 Anisotropy

The term “magnetic anisotropy” refers to the dependence of the magnetic properties on the direction in which they are measured (13 p. 123). Magnetization and hysteresis curves are affected by the magnitude and type of magnetic anisotropy (13 p. 123). Magnetic anisotropy is therefore an important factor when determining the suitability of a magnetic material for a particular application (13 p. 123).

2.6.1 Easy and hard axes

To explain the effect of magnetic anisotropy, we can take cobalt as an example: the crystallographic direction $[0001]$ of cobalt is called the *easy* axis, since it is the easiest direction to magnetize to saturation if an external field is applied in that direction (12 p. W38). The directions $[10\bar{1}0]$ and $[11\bar{2}0]$ in cobalt are considered to be *hard* axes since the saturation magnetization is most difficult to achieve in these directions (12 p. W38). Figure 10 shows a schematic illustration of the difference between these two terms. It should be noted that the final value of the magnetization is the same for both direction but the field required to reach the saturation value is distinctly different in each case.

The phenomenon that causes the magnetization to align itself along a preferred crystallographic direction is the magnetocrystalline anisotropy (13 p. 76). The crystal has higher energy when the magnetization points along the hard direction than along the easy direction. Further, the area between the hard and easy magnetization curves will give the magnetocrystalline anisotropy energy for the material (13 p. 77). As mentioned earlier, domains will try to form so that their magnetization points along the easy

crystallographic direction, so that the magnetocrystalline anisotropy energy minimizes (13 p. 78).

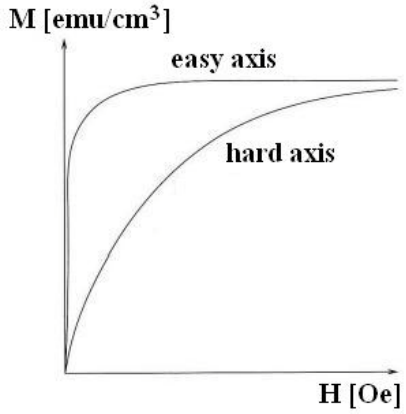

Figure 10. Schematic magnetization curves with the field oriented along the hard and easy direction (13 p. 77)

The anisotropy energy *E* can be calculated as

$$E = K_1 (\sin\theta)^2 + K_2 (\sin\theta)^4 + \cdots \qquad \text{(Eq. 6)}$$

where K_1 and K_2 are the anisotropy constants and θ is the angle between magnetization vector ***M*** and the easy axis (13 p. 126; 18 p. 8). The higher order terms are often neglected and only K_1 is usually considered when comparing various materials relative anisotropy energies (14 p. 16). In general, the lower number of easy magnetization axes in the crystal, the higher K_1 value which in turn means that it will be more difficult to magnetize in the hard direction (18 p. 8). Typical K_1 values for Sm_2Co_{17}, $SmCo_5$, and $Nd_2Fe_{14}B$ at room temperature are 3.3, 17.2, and 4.9 MJ/m^3, respectively (14 p. 17; 19). Notable, the anisotropy in all materials decreases with increasing temperature and at near Curie temperature there will be no preferred orientation for domain magnetization (13 p. 126).

2.6.2 Origin of magnetocrystalline anisotropy

The magnetocrystalline anisotropy has its roots in the electron spin-orbital coupling (13 p. 124). For example, when an external applied magnetic field tries to reverse the electron spin direction, the direction of the orbit spin must change as well (13 p. 124). The orbit in its turn is strongly tied to the crystal lattice which also influences the magnetization (13 p. 124). A much stronger external field is therefore required to force the orbit to align along a hard direction than if the orbit was to align along an easy axis.

In most materials this spin-orbit coupling is fairly week resulting in weak magnetocrystalline anisotropy. However, for the rare earth elements a strong spin-orbital coupling exists (13 p. 124). This means that once the sample has been magnetized, a large opposing field will be required in order to overcome the anisotropy and reverse the magnetization (13 p. 124). Rare earth elements are therefore a good candidate in applications where large coercive field is required (13 p. 124).

2.6.3 Shape anisotropy

Another factor which may also influence the magnetization is the shape of the sample. It can be shown that varying results are obtained when measuring the magnetization along different directions of the sample (13 p. 126). This is due to demagnetizing field that occurs inside the material when an external field is applied.

To explain what a demagnetization field is, suppose we have a prolate spheroid which is being magnetized by an applied magnetic field (13 p. 127). By definition, magnetic field

lines radiate from the north pole and at the south pole, resulting in the pattern of field lines shown in Figure 11 (13 p. 127). We can observe from the Figure 11 that the field inside the sample points in opposite direction to the applied external field. This internal field demagnetizes the magnet and thus called demagnetization field (13 p. 127).

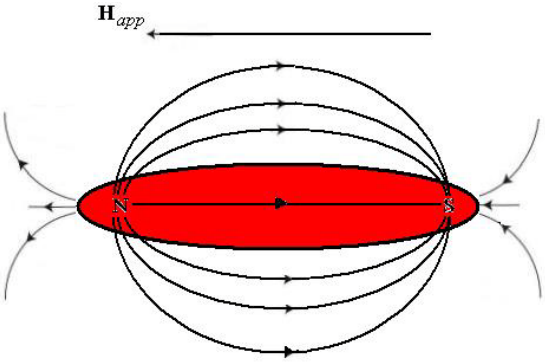

Figure 11. Schematic illustration of a demagnetization field for prolate spheroid. The applied field produces north and south poles (13 p. 127).

The demagnetizing field $\boldsymbol{H}_{\mathrm{d}}$ is given by the expression

$$\boldsymbol{H_d} = N_d \times \boldsymbol{M} \qquad \text{(Eq. 7)}$$

where N_{d} is the demagnetizing factor and $\boldsymbol{M}$ is the magnetization. The demagnetizing factor depends only on the geometry of the sample and some examples of the demagnetizing factors are listed in Table 3 (13 p. 128).

Table 3. ***Demagnetizing factors for various simple geometries*** **(11 p. 40).**

Geometry	N_d
Long cylinder	0
Sphere	0.333
Cylinder (l/d = 5)	0.040
Cylinder (l/d = 10)	0.0172

As a consequence of the demagnetizing field, the effective field acting inside the material $\boldsymbol{H}_{\text{eff}}$ will be smaller than the applied field $\boldsymbol{H}_{\text{app}}$ and a correction will be needed

$$\boldsymbol{H}_{eff} = \boldsymbol{H}_{app} - \boldsymbol{H}_{d} = \boldsymbol{H}_{app} - N_{\text{d}} \times \boldsymbol{M} \qquad \text{(Eq. 8)}$$

It can be seen from Eq. 8 that the demagnetization field will not have a significant impact on the $\boldsymbol{H}_{\text{eff}}$ when N_{d} is small. However, if N_{d} is large then most of the applied field goes into overcoming the demagnetization field.

2.7 Permanent Magnet

2.7.1 Hard and soft magnets

As discussed in chapter 2.6, the ferromagnetic materials can be classified as either hard or soft magnetic materials. Which group the magnet belongs to will usually depend on its coercivity. If the coercivity is below 12.5 Oe then it is classified as a *soft magnetic* material and in this group we find materials such as soft iron (11 p. 74). Magnets with coercivity exceeding 125 Oe are generally considered to be *hard magnetic* materials (11

p. 74). Sm-Co and Nd-Fe-B are magnets which belong to this group. The hard magnetic materials can also, based on their energy product $(BH)_{max}$, be divided into two main categories. If the magnet have a $(BH)_{max}$ ~0.25 Oe - 10 MGOe, it is considered to be a conventional magnet (12 p. W42). If the magnets energy product exceeds 10 MGOe, it is considered to be a high energy magnet (12 p. W43).

2.7.2 High energy hard magnetic materials

In the 1960's permanent magnets based on intermetallic compounds between Sm and Co were introduced (9). First the $SmCo_5$ phase was developed with great intrinsic magnet properties. Later, permanent magnets based on Sm_2Co_{17} were developed with an energy product of 32 MGOe (9; 14 p. 1). Nd-Fe-B alloy were developed in 1980's with an energy product of 37 MGOe (14 p. 1). However, through processing and alloy optimization this value has now increased up 55.9 MGOe (14 p. 1). The magnetic properties of $SmCo_5$, Sm_2Co_{17}, and other magnets at room and elevated temperature are listed in Table 4. Apart from high energy product, Sm-Co magnets also have a high Curie temperature. We can for example observe from Table 4 that the Sm-Co based alloys still have excellent magnetic properties even at elevated temperature. Speakers in audio systems, motors, computer peripherals, and elevated temperature applications are some applications where high-energy magnets are being used (12 p. W44).

Table 4. ***Magnetic properties for some common magnets*** **(20).**

	At 25°C			At 250°C			T_c [°C]
Materials	B_r [kG]	H_c [kOe]	$(BH)_{max}$ [MGOe]	B_r [kG]	H_c [kOe]	$(BH)_{max}$ [MGOe]	
$Nd_{14}Fe_{80}B_6$	13.79	13.70	45.2	8.65	0.63	1.52	310
Sm_2Co_{17}	11.67	10.69	31.5	10.65	8.68	25.4	805
$SmCo_5$	9.02	8.95	20.2	8.07	7.86	15.8	691
Alnico 5	12.84	0.74	5.3	12.22	0.73	5.18	840

2.7.3 Sm-Co alloys

Figure 11 shows the Co-rich section of the Sm-Co phase diagram. Numerous intermetallic compounds and other features can be interpreted from the phase diagram (9).

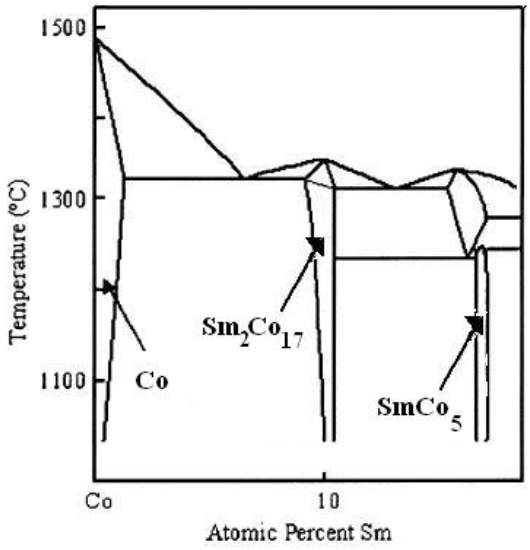

Figure 12. Co-rich section of the Sm-Co phase diagram (9; 21 p. 1240).

At higher Co content, the Sm_2Co_{17} compound exists. This compound forms as the prototypical rhombohedral Th_2Zn_{17} structure at lower temperatures and at higher temperatures as the hexagonal Th_2Ni_{17} structure (9). Two eutectics can be found in this Co-rich section; one between the Co and Sm_2Co_{17} phases at approximately 8 at.% and one between Sm_2Co_{17} and $SmCo_5$ (9). The Sm_2Co_{17} structure is related to $SmCo_5$ in that one-third of the Sm atoms in $SmCo_5$ are replaced by a pair of Co atoms (commonly referred to as dumbbells) (10). If the Co dumbbells are arranged on the lattice randomly the disordered $TbCu_7$-structure forms (10). This disordered $SmCo_7$ structure has the same unit cell as the $SmCo_5$ and is a metastable phase which can be stabilized through addition of alloying elements such as Ti or Zr or by rapid cooling (9; 10).

2.7.4 Manufacturing and properties of Sm-Co magnets

There are several ways to produce Sm-Co magnets and one of them is powder metallurgy. In powder metallurgy, the material is first prepared by standard melting techniques and then ground into fine powder followed by alignment using an external magnetic field. Next, the powder is pressed into the desired shape and sintered at elevated temperature (12 p. W43). The last step is to perform another heat treatment for improving the magnetic properties (12 p. W43).

The magnetic properties for the various high-energy magnets were listed in Table 4. However, Sm-Co possesses some features which stand out from the other high energy magnets: they have the best high-temperature performance of all rare earth magnets, good corrosion resistance, and no additional surface treatment is required (22) . It should also

be noted that sintered Sm-Co magnets are brittle and prone to cracking and might even fracture when exposed to thermal shock (23).

2.7.5 Improving the magnetic properties for Sm-Co alloys

Rare-earth, high-energy permanent magnets are currently the best performing permanent magnets used. But with higher demand for smaller and stronger magnets, the research ranges from discovering new magnetic materials to improving the properties of existing magnets. One breakthrough in improving existing magnets came with the discovery of single domain magnetism in the 1950's which demonstrated that the coercivity of powdered magnets increases with the reduction of particle size (4). The single-domain theory was discussed in chapter 2.4.4. From Figure 12 we can see that the coercivity started to increase with decreasing particle size, reaching a maximum at the single domain size. However, the coercivity started to decrease with further decreasing particle size and reached zero at the superparamagnetic particle size (4). Supermagnetism is a phenomenon in which the magnetic materials start to exhibit behavior similar to paramagnets below their Curie or the Néel temperature (24). The single-domain particle size for $SmCo_5$ and Sm_2Co_{17} has been reported to be about 1.6 and 0.66 µm, respectively (11 p. 319). This discovery motivated scientists to start research in nanophase hard magnetic materials and later nanocomposite magnets (4). A nanocomposite magnet consists of a fine mixture of magnetically soft and hard phases.

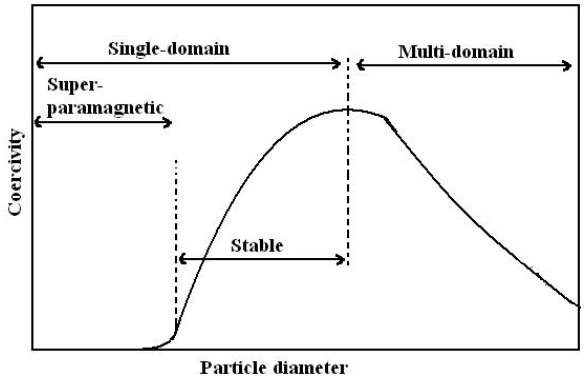

Figure 13. Schematic illustration of how the coercivity depends on the particle size (4).

2.7.6 Nanocomposite magnets

Nanocomposite magnets, as mentioned earlier, consist of a fine mixture of magnetically hard and soft phases. The hard phase is characterized by high coercivity, low remanance, and high energy product while the soft phase is characterized by having a high magnetization, high remanance, and low coercivity. Mixing these two phases can result in that the spins of the soft phase interact across grain boundaries and be locked into alignment with the hard phase. This procedure is termed *exchange coupling*. In strong exchange-coupled materials the soft phase is completely coupled with the hard magnetic phase, resulting in the reversal of the hard and soft phase occurring simultaneously (25). However, it is necessary that the soft phase is of nanoscale dimensions, approximately twice the width of the domain wall in the hard phase, so that its magnetic moments are exchange coupled with the hard phase (9; 26). The critical dimension of the soft phase, below which the soft phase is coupled to the hard phase, is calculated by (26):

$$\delta_h = 2\pi\sqrt{A_h/K_h} \qquad \text{(Eq. 9)}$$

where A_h and K_h are the exchange and anisotropy constants of the hard magnetic phase, respectively. Notably, the larger the amount of soft phase, the higher the magnetization at the expense of significant lower coercivity due to lower amount of hard phase (4). It has been shown that the energy product decreases significantly if the soft phase exceeds ~15 vol. % of the nanocomposite (27). The hysteresis loops for nanocomposite are usually characterized by being smooth and the remenent ratio M_r/M_s exceeding the Stoner-Wohlfarth limit of 0.5, which is the highest limit for isotropic magnets (28; 29). Further, it is suggested that for exchange coupling to influence the overall magnetic properties, the grain/particles size must below a critical threshold, usually on the order of 30 - 50 nm (28).

Methods to develop nanocomposite magnets

One way to develop a nanocomposite structure has been to make the alloys into amorphous structure and then anneal them to crystallize them into the desired microstructure (4). Problems that can occur with this method are that the obtained microstructure is not very uniform and the size of the soft phase tends to be too large for optimum exchange coupling (4).

Currently two techniques have been successful implemented for producing nanocomposite magnets: melt spinning and mechanical alloying/milling. How the melt-spinning and mechanical alloying/milling are influencing the nanocomposite and its properties will be discussed below. However, both processes will be discussed more thoroughly in chapter 3.

In general, melt-spinning is a process where a melt is rapidly solidified onto a rotating wheel, producing ribbons with nano-crystalline grain structure. The speed of the wheel controls the cooling rate and can therefore be used to control the resulting grain size. For example, the scale of the Co in the eutectic alloy was decreased from 50 nm to 25 nm as the wheel speed was increased from 20 to 40 m/s (30). A breakthrough in the development of nanocomposite magnets came in 1980's when large coercivity on melt-spun Pr-Fe-B(Si) and Nd-Fe-B alloys were obtained (4). It was believed that the large coercivity obtained for both systems were related to the nanoscale sized phase (4). This discovery led to many other alloys, such as Sm-Co, being synthesized with the melt-spinning technique, resulting in nanoscale microstructure and large values of coercivity (4).

The other common technique used to develop nanocomposite magnets have been mechanical alloying/milling. The term "mechanical alloying" is restricted to the formation of alloys or mixtures by mechanical means whereas mechanical milling describes the process of milling powders to reduce the particle size or for the refinement of structure (5; 31 p. 254). Mechanical alloying/milling combined with subsequent heat treatment has shown to produce extremely fine microstructure and a high coercivity similar to those produced by rapid solidification. This method was first shown for Nd-Fe-B alloy and later successfully applied to hard magnetic alloy systems such as Sm-Co (6; 8). An extensive study was performed by Chen *et al.* (7) on Sm_2Co_{17}-based mechanically milled powders with emphasis on the structure, microstructure, and magnetic properties developed during the different stages of the mechanical milling. The result obtained for

the as-milled powders showed that with increasing milling time the coercivity increased with milling time reaching a maximum due to the grain size refinement. Next, with further increasing milling time the coercivity decreased due to disappearance of the 2:17 phase and formation of the amorphous phase (7). However, it was found that high coercivity could be obtained in over-milled powders by an appropriate subsequent annealing which will crystallize the amorphous phase.

Chapter 3. Experiments

3.1 Sample preparation and arc-melting

Background

An arc-melter can be used whenever it is desired to create a solid homogenous ingot from metallic elements. The first step is to place the starting materials on the copper crucible. To ensure an inert environment, the chamber will then be evacuated and backfilled several times with Ar. Then, the water will be turned on to cool and keep the crucible cooled during the process, so that the crucible does not melt together with the compound. While pointing the electrode on the sample, an electric arc will be created resulting in the sample heating until it is completely melted.

Experimental procedures

The samples $Sm_{10.5}Co_{89.5}$ and Sm_8Co_{92} [atomic percent] had to be converted first to weight percent by the composition conversion (12 p. 71):

$$W_{Co} = \frac{C'_{Co}A'_{Co}}{C'_{Co}A_{Co}+C'_{Sm}A_{Sm}} \times 100 \qquad \text{(Eq. 10)}$$

$$W_{Sm} = 100 - W_{co} \qquad \text{(Eq. 11)}$$

where W_x is the weight percent, C'_x is the atomic percent, and A_x is the atomic weight [g/mol]. The calculated conversions are listed in Table 5

Table 5. ***Conversion from atomic to weight percent and density for $Sm_{10.5}Co_{89.5}$ and Sm_8Co_{92}.***

Composition	C'_{Co} [at.%]	C'_{Sm} [at.%]	A_{Co} [g/mol]	A_{Sm} [g/mol]	W_{Co} [wt.%]	W_{Sm} [wt.%]
$Sm_{10.5}Co_{89.5}$	89.5	10.5	58.9332	150.36	76.96	23.04
Sm_8Co_{92}	92	8	58.9332	150.36	81.84	18.16

A total of four samples where arc-melted: $2 \times Sm_{10.5}Co_{89.5}$ and $2 \times Sm_8Co_{92}$. The Sm-Co alloys were prepared from pure Sm and Co components. A 5 wt.% of extra Sm was added to compensate for Sm evaporation loss during the melting and melt spinning. The elements were then placed on the copper crucible. The ingots were re-melted two times to insure homogeneity. The ingot was weighed afterwards to monitor weight loss.

3.2 Melt Spinning

Background

Melt-spinning is a technique where the sample is melted and rapidly solidified against a rotating copper wheel. The ingot is first placed in a quartz crucible containing a small opening at the bottom. The crucible is then positioned inside the melt-spin chamber followed by evacuation and backfilling with Ar several times. RF induction heating is used to melt the ingots. The temperature is monitored using a two-color pyrometer. The melt will be ejected through the small opening, once the desired temperature is reached, onto the copper wheel which will solidify the liquid. The resulting product, ribbon, is then thrown off the wheel. A schematic illustration of the melt spinner is shown in Figure 14.

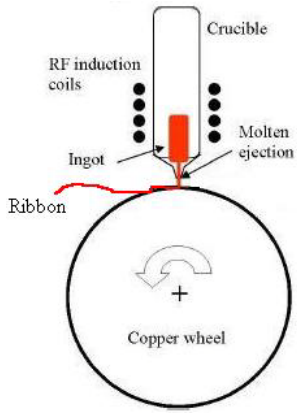

Figure 14. Schematic illustration of melt-spinning (14 p. 25)

Experimental procedures

A small hole was formed at the bottom of the quartz crucible by using SiC, followed by rinsing and weighing of the crucible. The arc-melted ingot was then placed inside the crucible and inserted in the chamber between the RF induction coils. The velocity of the copper wheel was set to either 20 m/s or 40 m/s, see Table 6. The ingot was ready to be fired out from the crucible once it had melted completely. The ribbons were weighed afterwards, together with the material remaining from the ingot and inside the crucible.

Table 6. ***The compositions and their respective melt-spin velocity.***

Composition	Melt-spin velocity [m/s]
$Sm_{10.5}Co_{89.5}$	20
$Sm_{10.5}Co_{89.5}$	40
Sm_8Co_{92}	20
Sm_8Co_{92}	40

3.3 Mechanical Milling

Background

Mechanical milling is a process where the physical sizes of the coarse solid particles are reduced to micro-structural level (5). Planetary mill, vibratory mill, tumbling mill, and shaker mill are some examples of various types of mechanical milling apparatus that exist (5). For the research reported in this thesis, the shaker mill with the *agitation method* was used and therefore is discussed more fully as follows.

First the sample and milling balls are placed together in a vial. In the agitation method the vial be moving back and forth with the sample and milling balls inside (5). The balls will in every swing hit the end of the vial with some amount of sample trapped between them and the wall. At the moment of collision, impact energy will be generated, resulting in deformation, fracture, and also welding of the sample particles (5). This is schematically illustrated in Figure 15

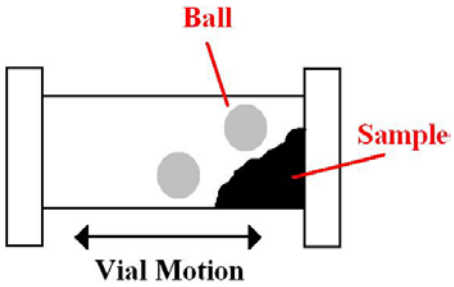

Figure 15. Illustration of the motion of the sample and the vial (5).

Several parameters must be taken in consideration when mechanical milling. One of them is the ratio of the amount of milling balls to sample (often in unit mass). The ratio

should be chosen so that maximum amount of milling balls is in contact with maximum amount of sample (5).

Reports from different investigators have shown that 80-90% of the energy generated during milling is transformed into heat and this will subsequently raise the temperature of the powder (5; 32 p. 121). Some consequences of the temperature rise are oxidation of the powder and crystallization of the amorphous phases (32 p. 135). Precautions should therefore be taken to minimize the temperature rise and one way to do this is by using fan cooling which have proven to be effective (32 p. 135). Another solution is to mill the powder for a predetermined time, interrupt milling until the vial cools down to some reasonable temperature and then resume milling (32 p. 135).

Another major concern in the mechanical milling process is powder contamination contributed from wearing and tearing of the milling tools (32 p. 385). To minimize the powder contamination, one could use milling tools made of the same material which are harder than the powder being milled (32 p. 401).

Experimental Procedure

The sample preparation for mechanical milling was carried out inside an Ar-filled glove-box. The melt-spun ribbons where placed into the hardened steel vial together with the hardened steel balls. The ball-to-sample weight ratio was set to 3:1. The vial was then placed in the SPEX 8000 miller, which started to move the vial back and forth. The samples were milled and cooled in 10 minute intervals, to avoid thermal reaction, up to 6

hours. Approximately 0.17 gram of the milled powder where removed from the vial at different time intervals for further examination in the X-ray diffraction and alternating gradient force magnetometer.

3.4 X-ray diffraction

Background

X-ray diffraction (XRD) is commonly used to characterize a material's crystal structure, grain size, phases present, and texture (14 p. 26).

Inside the X-ray tube, the cathode produces electrons with high velocity which will upon impact with the anode lose their energy and manifest as X-ray (33 p. 5). The X-ray beam will then encounter the crystal lattice of the sample producing scattered X-ray which will be collected by the detector for analyzation (14 pp. 26-29). X-ray is an electromagnetic radiation which can be found between γ-rays and ultraviolet radiation in the electromagnetic spectrum (33 p. 3).

Determination of phases and grain size

Determination of phases in the sample is usually done by comparing the obtained diffraction pattern with existing data in X-ray charts.

When it comes to determining the grain size of a sample, certain steps must be taken first. If the sample is crystal, the XRD peak will be characterized by a sharp peak (33 p. 209). For samples which are not crystals, the diffraction peaks are broadened mainly due

to three factors: Instrumental effect, crystallite size and lattice strain (33 p. 208). These factors have to be subtracted from the obtained XRD peak which can be done in several steps (33 pp. 211-215):

1. *Instrumental effect:* To reduce the instrumental effect, one has to take the width w [radians] of the obtained XRD peak and subtract it with a known standard w_{std} (narrowest peak that is possible to be measured). This will give the full width at half maximum (FWHM) of the diffracted peak B

$$B = \sqrt{w^2 - w_{std}^2} \qquad \text{(Eq. 12)}$$

2. *Crystallite size*: Scherrer formula has derived an expression for broadening of XRD peaks due only to small crystallite sizes

$$B = \frac{0.9\lambda}{L\cos\theta} \qquad \text{(Eq. 13)}$$

where L is the grain diameter[m], λ is the wavelength [m], θ is the location of the peak [radians], and B is the crystallite size.

3. *Lattice strain*: The lattice strain in the material, which also causes broadening of the diffraction peaks, can be represented by the relationship

$$B_{strain} = \eta \tan\theta \qquad \text{(Eq. 14)}$$

where η is the strain in the material.

4. The width of the diffraction peak B_r is the sum of the widths from crystallite size and lattice strains

$$B_r = B + B_{strain} \qquad \text{(Eq. 15)}$$

Substituting (Eq. 13) and (Eq. 14) into (Eq. 15) will give

$$B_r \cos\theta = \frac{0.9\lambda}{L} + \eta \sin\theta \qquad \text{(Eq. 16)}$$

5. The last step is to plot $B_r \cos\theta$ against $\sin\theta$ which is schematically illustrated in Figure 16.

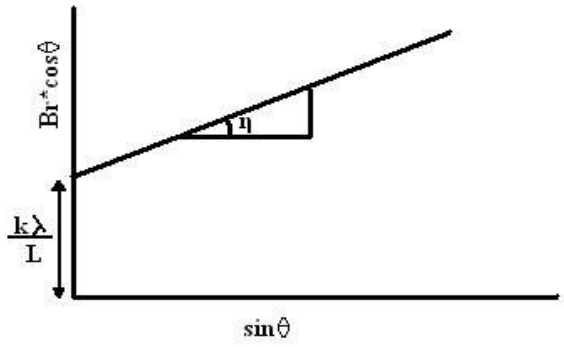

Figure 16. Plot of $B_r \cos\theta$ versus $\sin\theta$, indicating that the intercept $\frac{k\lambda}{L}$ and slope η can be used to calculate the crystallite size L.

From the Figure 16, we see that the plot gives a straight line with slope η and intercept $\frac{k\lambda}{L}$. The intercept will increase with decreasing crystallites size. Further, the lesser the slope of the line, the lower the amount of strain in the material. The size of the crystallite can be calculated from the intercept according to

$$L = \frac{0.9\lambda}{B_r \cos\theta} \qquad \text{(Eq. 17)}$$

Experimental procedure

Rigaku Multiflex was used for the XRD-measurement. The Rigaku uses a Cu-Kα radiation and θ-θ geometry which means that the sample is held stationary while the source and detector rotate (14 p. 29). The samples were prepared on a zero background holder and placed into the XRD. The XRD measurement was done between 20°- 60° with a scan speed of 0.5°/min.

The obtained data was then observed in the computer program *Origin 7*. Three peaks where chosen from the XRD measurement for calculating the grain size and to reduce the instrumental effect, a known standard measurement of Si was used.

3.5 Alternating gradient force magnetometer

Background

As discussed in chapter 2.6 the coercivity, remenance, saturation magnetization, and energy product can be derived from the hysteresis loop. A hysteresis loop can be obtained by several techniques but the one which was used in this thesis was an alternating gradient magnetometer (AGFM).

The AGFM consist of two gradient coils, a probe, and an extension rod attached to a piezoelectric element, see Figure 17 (34). The sample is mounted on the piezoelectric element and placed between the gradient coils. The sample is magnetized by a dc field

and is simultaneously subjected to a small alternating field gradient (35). The alternating field gradient exerts an alternating force on the sample, proportional to the magnitude of the field gradient and to the magnetic moment of the sample (35). The resulting deflection of the rod is measured by the voltage output of the piezoelectric element (34; 35). This amplitude will depend on the force experienced by the sample, and if the gradient is known the magnetic moment can be calculated (11 p. 74; 34).

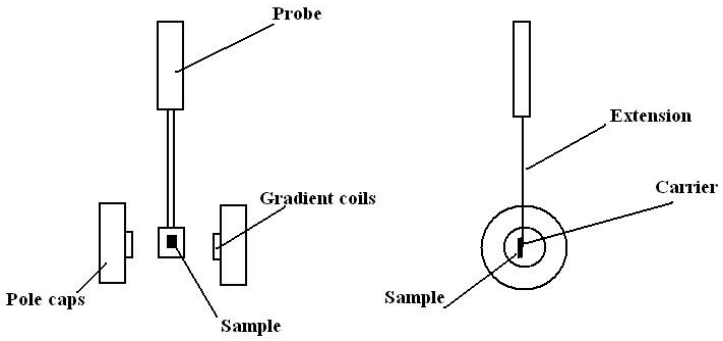

Figure 17. Schematic illustration of the front and side view of the AGFM (34).

Experimental procedure

Small pieces of a plastic straw were cut out and used as holder for the powder. The powders for each sample were measured to be around 1.0 - 3.0 mg. The powders were then mixed together with epoxy resins into the holders. The samples were first pulse magnetized in a 30 kOe field to assure saturation of the samples before the magnetic measurement. The AGFM system used was Princeton Measurements Corporation of the Model 2900 Micromag^{TM} System and a 12 kOe field was applied on the samples.

3.6 Scanning electron microscope

Background

The scanning electron microscope (SEM) is an analytical instrument used for imaging at higher magnifications than possible in optical microscopy or when a high depth of field is required (36 p. 8). In the SEM an electron beam is focused into a fine probe and subsequently rastered over a small rectangular area where it will interact with the sample (36 p. 8). The beam will then create various signals (secondary electrons, internal currents, etc.) which will be collected by a detector (36 p. 8). The images produced is highly magnified and with much greater depth of field than a traditional microscopic image (36 p. 8).

Experimental procedure

The powders were prepared on a double sided carbon tape and inserted into the Hitachi S4700 Field-Emission SEM. The particle sizes where then measured from the images using ImageJ (37).

Chapter 4. Results and Discussion

4.1 X-ray diffraction and analysis

The progressive development of the structure and microstructure of the samples at different milling times were examined by XRD. The XRD results for the $Sm_{10.5}Co_{89.5}$ melt-spun samples are presented in Figure 18. The only phase present in the as-melt-spun samples was $SmCo_7$ having the $TbCu_7$-type structure. No signs of the ordered Sm_2Co_{17} phase were observed in x-ray diffraction patterns of either sample. This is believed to be because of the high wheel speed used during melt spinning. At the initial stage of the mechanical milling, the XRD peaks for both samples became broader which indicates a decrease in grain size due to the high-energy mechanical collision between the powders and the steel balls. However, the samples remained crystalline, as the characteristic peaks of $TbCu_7$-type structure were always present. FCC-Co developed in both samples with further increase in milling time, likely due to Sm losses during milling, despite the aforementioned precautions. A large fraction of FCC-Co appeared for the 6 h milled $Sm_{10.5}Co_{89.5}$ melt-spun at 20 m/s sample for which no good explanation exists.

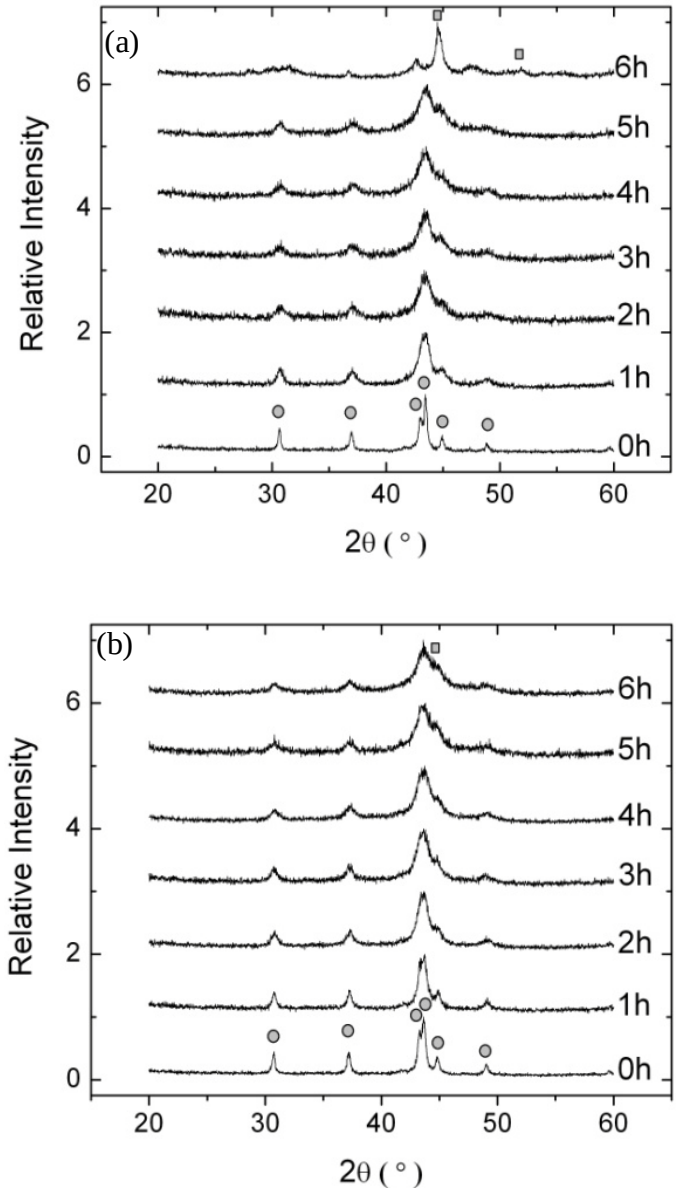

Figure 18. XRD patterns of $Sm_{10.5}Co_{89.5}$ melt-spun at (a) 20 m/s and (b) 40 m/s as a function of milling time. The only phase existing in the as-melt-spun (0 h) samples was the disordered $SmCo_7$ (circle). However, with increasing milling time FCC-Co (square) started to develop.

For the Sm_8Co_{92} the $TbCu_7$-type structure and FCC-Co were the phases existing in the as-melt-spun samples (Figure 19). The presence of FCC-Co in the as-melt-spun samples is believed to be due to higher Co content and neither here were there any signs of the ordered Sm_2Co_{17} phase. With increasing MM time, the intensity of XRD peaks for both Sm_8Co_{92} samples decreased and became broader which indicates a decrease in grain size in the powders. The samples remained crystalline as the characteristic peaks of $TbCu_7$-type structure and FCC-Co phase were always present. No significant loss of Sm was detected in these samples.

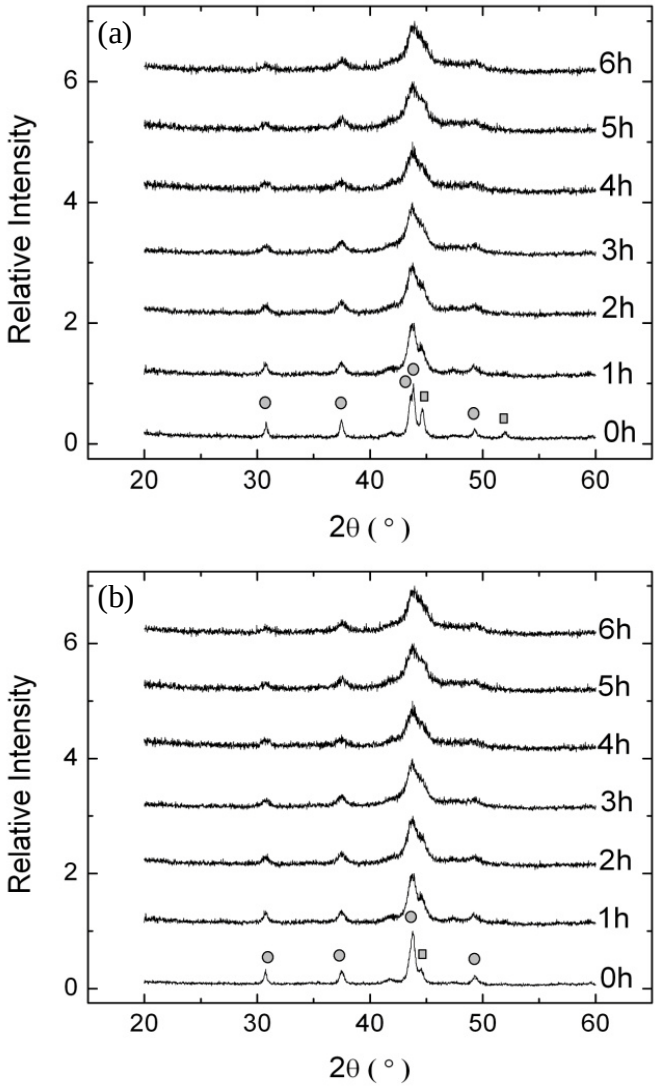

Figure 19. XRD patterns of Sm_8Co_{92} melt-spun at (a) 20m/s and (b) 40m/s as a function of of milling time. The disordered $SmCo_7$ (circle) and FCC-Co (square) phases were present in the as-melt-spun (0 h) samples and throughout the milling process.

The grain size for both compositions was calculated from the x-ray diffraction patterns using the Scherrer equation after accounting for strain (Equations 12-16). Figure 20 shows the grain size as a function of milling time for all four samples. The grain size for both the $Sm_{10.5}Co_{89.5}$ melt-spun showed to be ~70 - 80 nm. For the Sm_8Co_{92} melt-spun at 20 m/s the observed grain size was ~40 nm while for the Sm_8Co_{92} melt-spun at 40 m/s the obtained grain size was ~400 nm. The grain size for both compositions decreased as expected with increasing milling time, reaching grain sizes between 10 - 20 nm. The grain size for the powdered 6 h milled $Sm_{10.5}Co_{89.5}$ melt spun at 20 m/s, could not be calculated with the above equations due to the XRD peaks chosen for calculation were to broad.

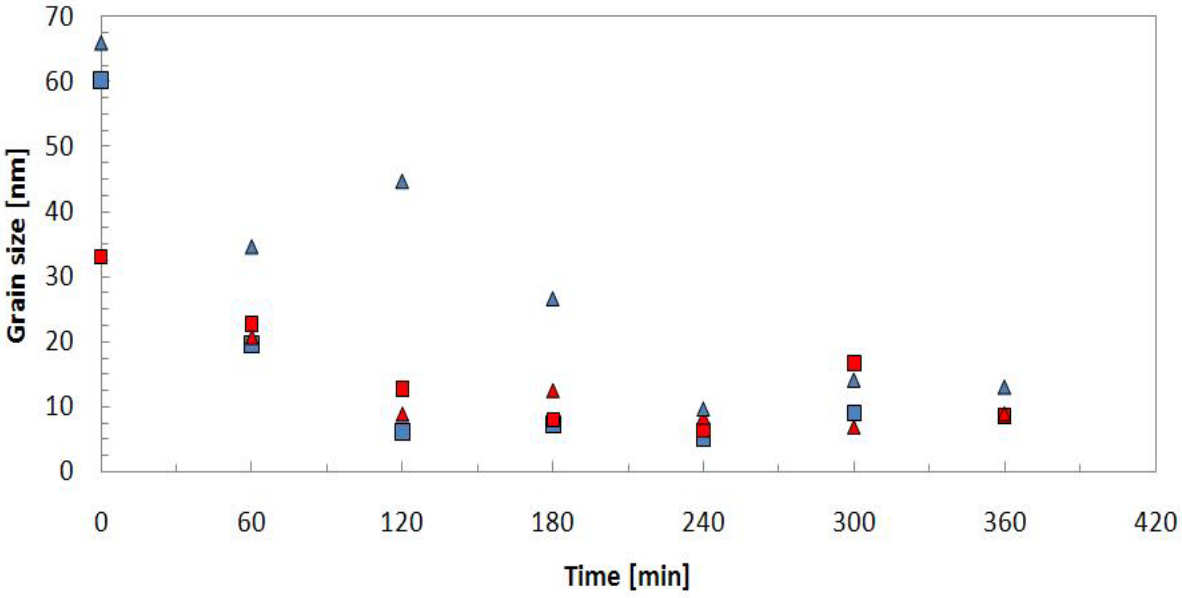

Figure 20. The grain size as a function of milling time. The grain size for $Sm_{10.5}Co_{89.5}$ melt-spun at 20 m/s (blue square) and 40 m/s (blue triangle) and Sm_8Co_{92} melt-spun at 20 m/s (red square) and 40 m/s (red triangle) decreased with increasing milling time as a result of ball/powder collision. Sizes as low as 10 - 20 nm were obtained.

4.2 Magnetic Properties

Figures 21 and 22 shows the hysteresis loops for the four as-melt-spun samples. The samples showed, except for the $Sm_{10.5}Co_{89.5}$ melt spun at 20 m/s, a typical smooth hysteresis loop suggesting single phase behavior with fine and uniform grain size in the samples. The "neck" observed in the magnetization curve of $Sm_{10.5}Co_{89.5}$ melt spun at 20 m/s suggests two-phase behavior in this sample. The initial assumption was that this "neck" occurred due to regions of soft phase (FCC-Co) exist and that they are easily reversed at low applied field. This assumption had to be abandoned since no FCC-Co was detected in the as-melt-spun samples (Figure 18). Instead, it was believed that the "neck" occurred due to different microstructures in the ribbons. It has been observed in ribbons melt-spun at low wheel speeds (10 m/s) that different microstructures are obtained on the wheel and non-wheel side of the ribbon (38). Different microstructures might therefore, due to the low wheel speed, exist in our sample and react in the "neck way" when a magnetic field is applied. However, to confirm this theory, further microstructure analysis is necessary.

Coercivity values of ~1.13 and ~1.75 kOe were obtained for $Sm_{10.5}Co_{89.5}$ melt spun at 20 and 40 m/s, respectively. It is believed that the higher coercivity for as-melt-spun $Sm_{10.5}Co_{89.5}$ melt spun 40 m/s is due to the higher wheel speed. Higher wheel speed, as mentioned earlier, results in smaller grains which consequently led to higher coercivity (30).

The coercivity obtained for as-melt-spun Sm_8Co_{92} was lower than for the $Sm_{10.5}Co_{89.5}$ which was expected since the Sm_8Co_{92} contains larger fraction of FCC-Co. It is known

that the coercivity drops with increasing soft magnetic phase fraction (9). The as-melt-spun Sm_8Co_{92} melt-spun at 20 and 40 m/s showed a coercivity of ~0.93 and 1.01 kOe, respectively. Further, the coercivity did not differ significantly between the Sm_8Co_{92} samples even though the difference in grain size was very large (Figure 20). It is believed that in these samples the grain size plays a smaller role since a larger fraction of FCC-Co is present and the soft phase will therefore control the reversal process.

The remanance ratio M_r/M_s for the $Sm_{10.5}Co_{89.5}$ melt spun at 20 m/s was slightly above the Stoner-Wohlfart limit of 0.5, indicating that exchange coupling exist between the nanograins. This result contradicts the "neck"-result (see above) and a hypothesis could be that the sample contains regions where the phases are exchange coupled but the regions themselves are not coupled to each other. Further, the M_r/M_s obtained for $Sm_{10.5}Co_{89.5}$ melt-spun at 40 m/s were ~0.5 and lower for both Sm_8Co_{92} samples. This suggests that there is no exchange coupling in these samples.

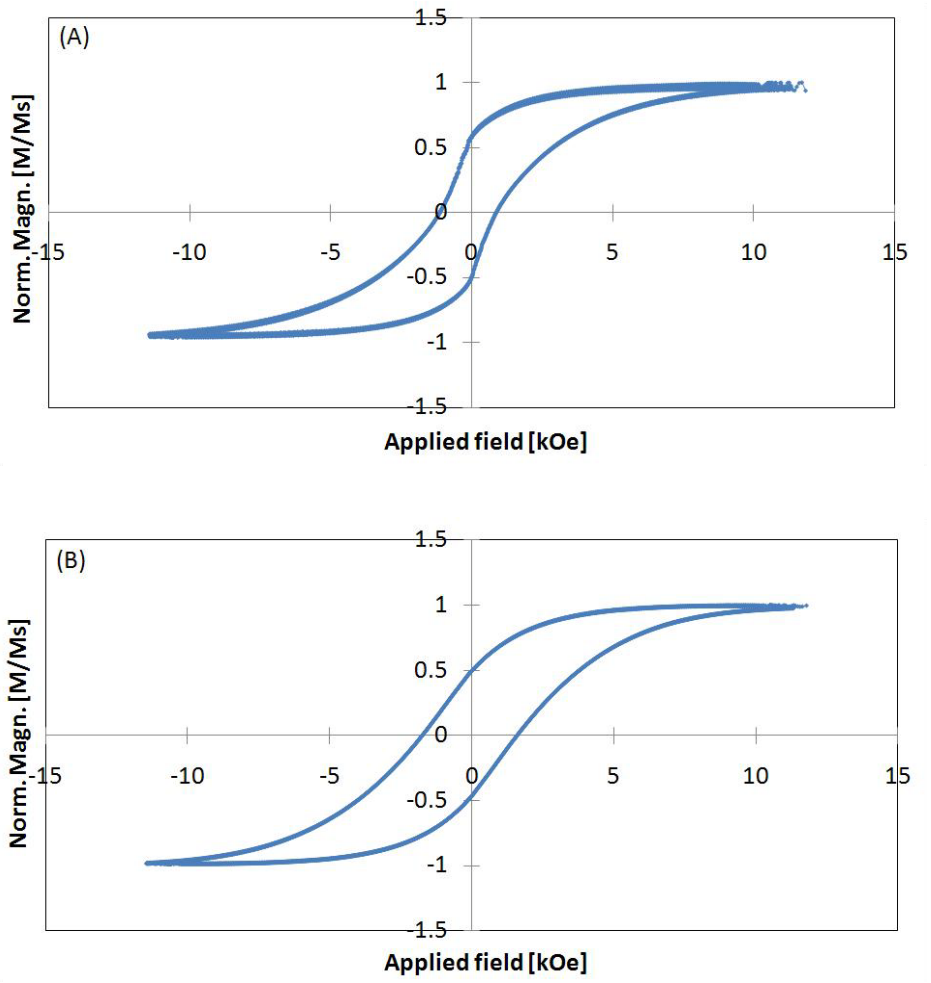

Figure 21. Hysteresis loops of as-melt-spun $Sm_{10.5}Co_{89.5}$ melt-spun at (A) 20 m/s and (B) 40 m/s.

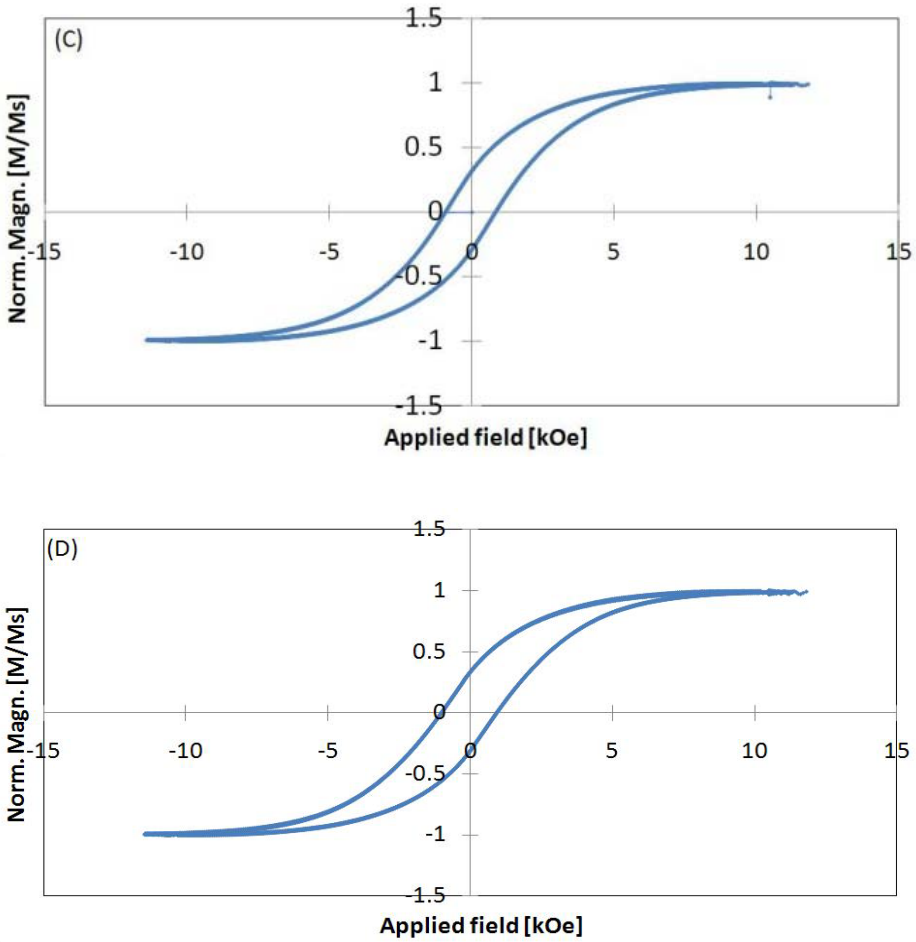

Figure 22. Hysteresis loops of as-melt-spun Sm_8Co_{92} melt spun at (C) 20 m/s and (D) 40 m/s.

We observed that when starting to mechanical milling all four samples, the coercivity and M_r/M_s increased with increasing milling time. This enhancement can be connected with results obtained in XRD measurement, i.e. both coercivity and remanance ratio increased with decreasing grain size. The hysteresis loops for as-melt-spun, 2 and 4 h milled for all four samples are shown in Figures 23 and 24. For the $Sm_{10.5}Co_{89.5}$ melt-spun at 20 and 40 m/s, the coercivity and remanance ratio increased significantly with increasing milling time. The remanance ratio for both samples exceeded the 0.5 limit, suggesting that exchange coupling now exist between the grains. This is clearly seen in

the $Sm_{10.5}Co_{89.5}$ melt-spun at 20 m/s where the “neck” could still be observed after 2 h of milling but disappeared after 4 h milling. The resulting hysteresis loop for 4 h milled $Sm_{10.5}Co_{89.5}$ melt-spun at 20 m/s became smooth; suggestion fine and uniform exchange coupled grains exist in the sample.

For the Sm_8Co_{92} melt-spun at 20 and 40 m/s both the coercivity and remanance ratio increased very slightly with increasing milling. The samples still behaved as a single magnetic phase with its smooth hysteresis loops. It is believed that, despite decreasing grain size in the sample, the enhancement did not occur due to high Co content.

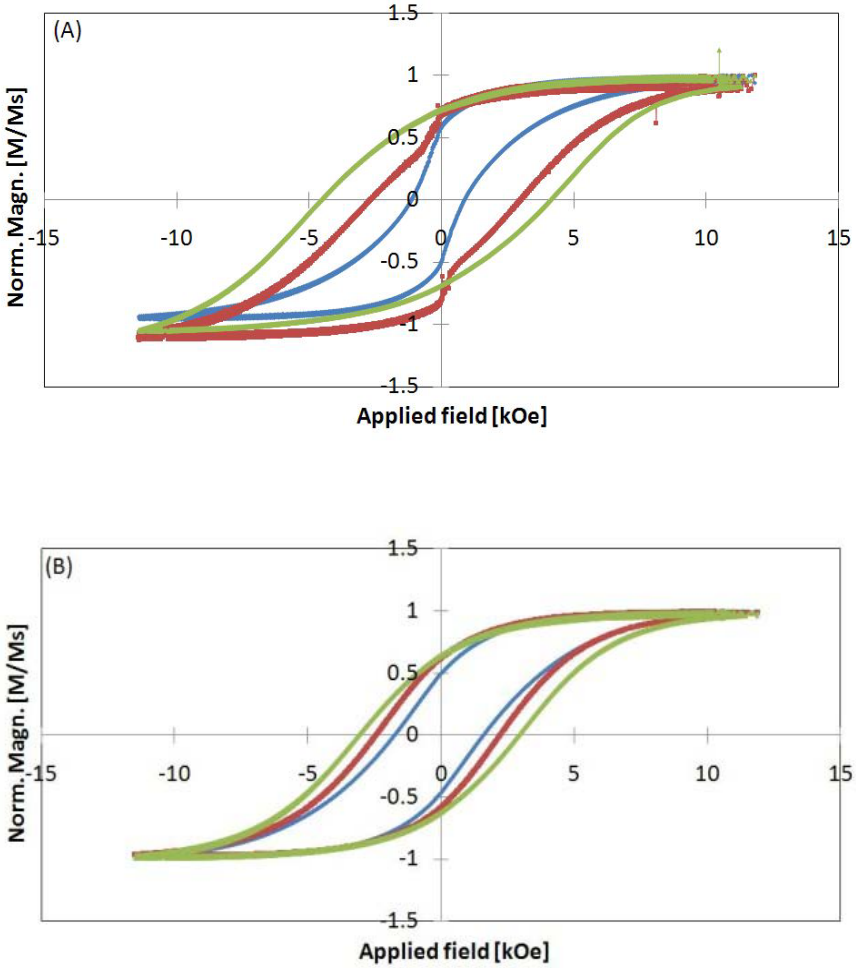

Figure 23. Hysteresis loops of as-melt-spun (blue), 2 h (red) and 4 h (green) for $Sm_{10.5}Co_{89.5}$ melt spun at (A) 20 m/s and (B) 40 m/s. The coercivity and remanance ratio increased significantly with increasing milling time for both samples.

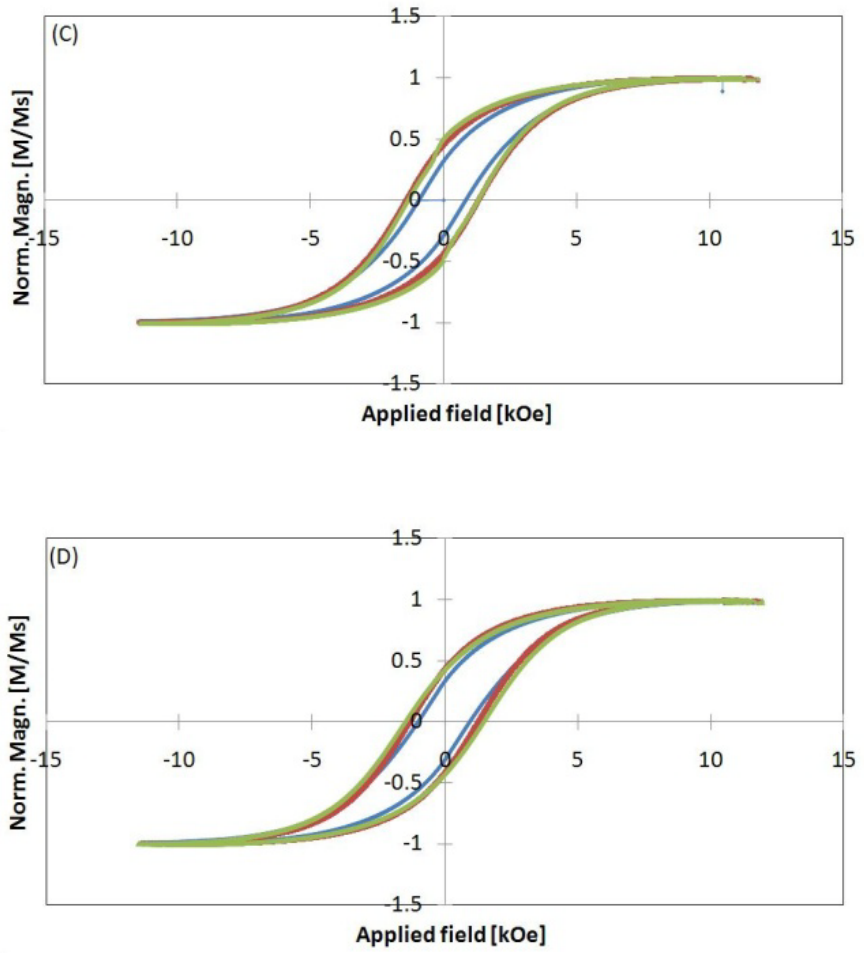

Figure 24. Hysteresis loops of as-melt-spun (blue), 2 h (red) and 4 h (green) for Sm_8Co_{92} melt spun at (C) 20 m/s and (D) 40 m/s. The coercivity and remanance ratio increased very slightly for both samples.

The coercivity for all four samples initially increased with increasing milling time before reaching a plateau value. Figure 25 shows the coercivity for all four samples as a function of milling time. Coercivity as high as ~4.6 and 3 kOe was obtained for $Sm_{10.5}Co_{89.5}$ melt spun at 20 and 40 m/s, respectively. Further microstructure analysis is

necessary to explain the difference in coercivity since both samples had similar grain sizes (Figure 20).

The coercivity for both Sm_8Co_{92} samples increased slightly with increasing milling time, reaching as high as ~1.7 kOe. The lower coercivity value of Sm_8Co_{92} compared to the $Sm_{10.5}Co_{89.5}$ is believed to be due to higher Co content.

Notably, we observe that for $Sm_{10.5}Co_{89.5}$ melt-spun at 20 m/s a sudden drop in coercivity occurs in the 6 h milled sample. This sudden drop is believed to be related to the formation of the large fraction of FCC-Co at 6 h milling (Figure 18).

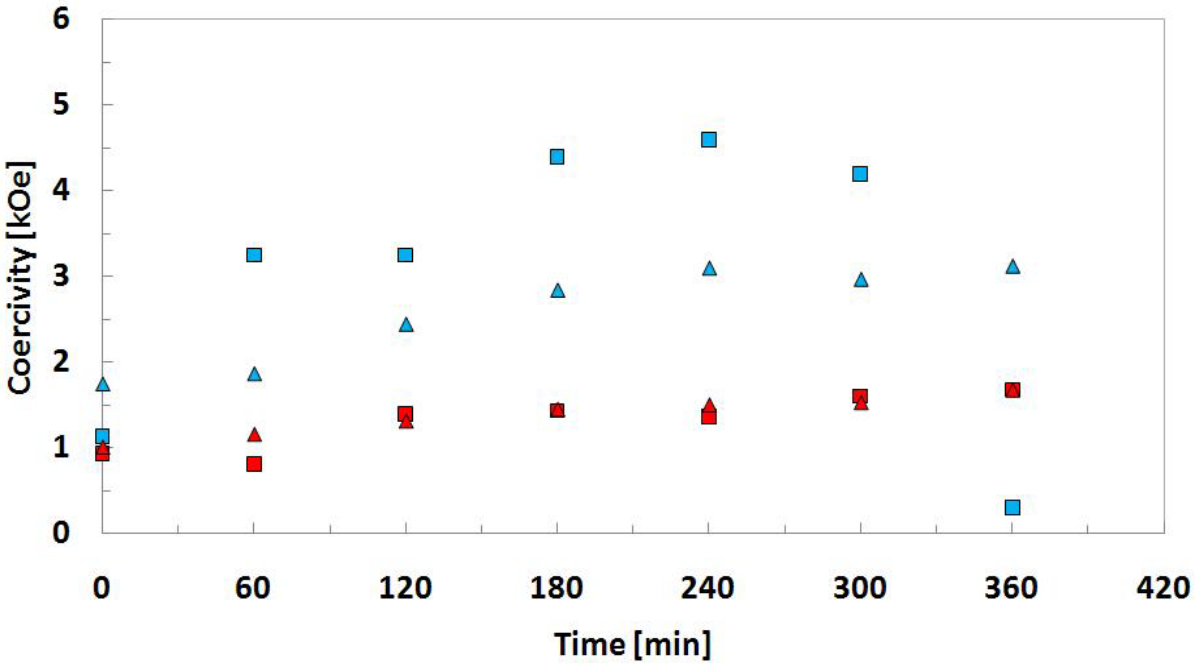

Figure 25. The coercivity as a function of milling time for powdered $Sm_{10.5}Co_{89.5}$ melt-spun at 20 m/s (blue square) and 40 m/s (blue triangle) and powdered Sm_8Co_{92} melt-spun at 20 m/s (red square) and 40 m/s (red triangle). It can be seen that the coercivity increased for all samples with increasing milling time, reaching a plateau value. Highest coercivity recorded was ~4.6 kOe.

4.3 Particle Morphology

Figure 26 shows the scanning electron micrographs for as-melt-spun, 2, and 4 h milled samples for $Sm_{10.5}Co_{89.5}$ melt-spun at 20 m/s. First of all, it is necessary to distinguish between the particle size and grain size since they are not equal to each other. A micron-scale particle can contain many smaller nanosized grains (39). This was also observed in our samples. The small grains inside a particle is thought to have been formed either from plastic deformation of the particles during milling or from joining (welding) of small nanoparticles (39).

The particle distribution for the respective samples can be seen in Figure 27. It was found that a broad particle size distribution exist in the milled powder with an average particle size around a few microns. The average particle size decreased slightly with increasing milling time. This morphology and particle distribution was similar for the other samples.

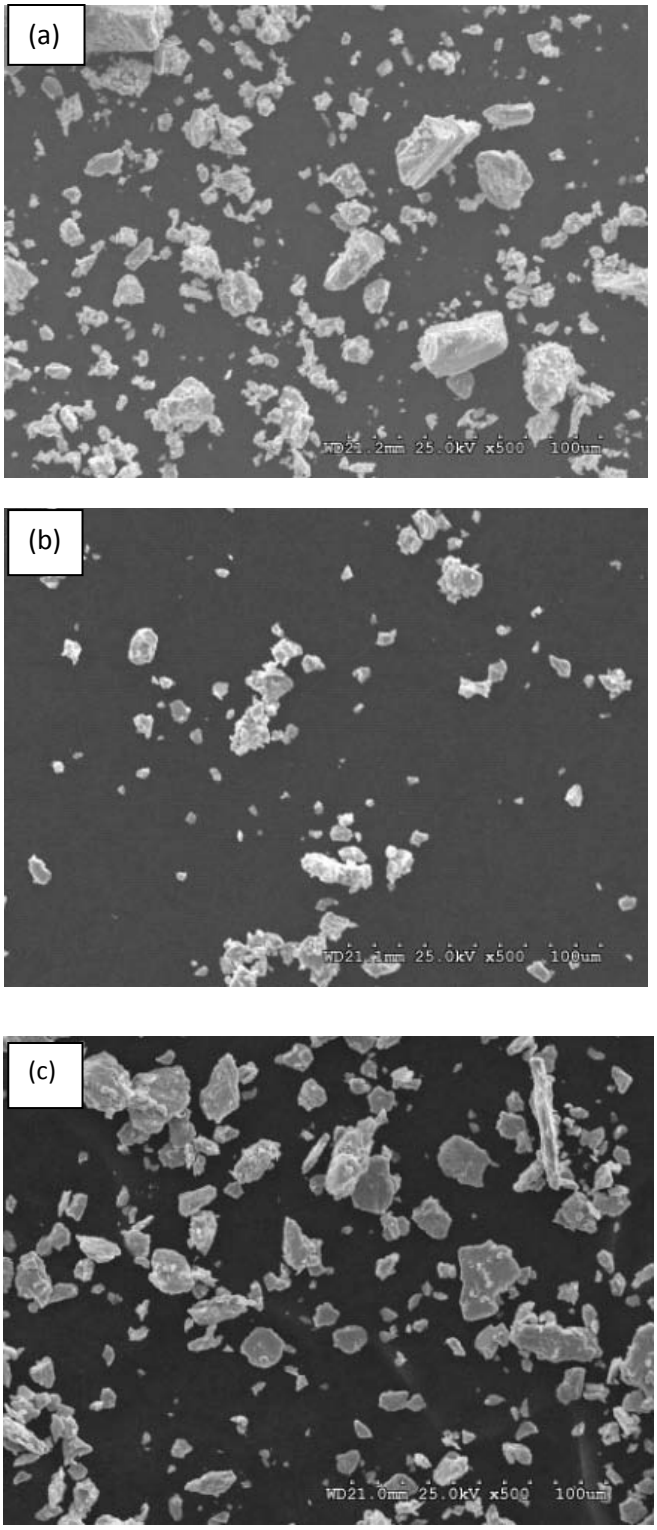

Figure 26. SEM images of (a) as-melt-spun (b) 2 and (c) 4 h milled $Sm_{10.5}Co_{89.5}$ melt-spun at 20 m/s, showing micron-size particles containing nanoscale grains.

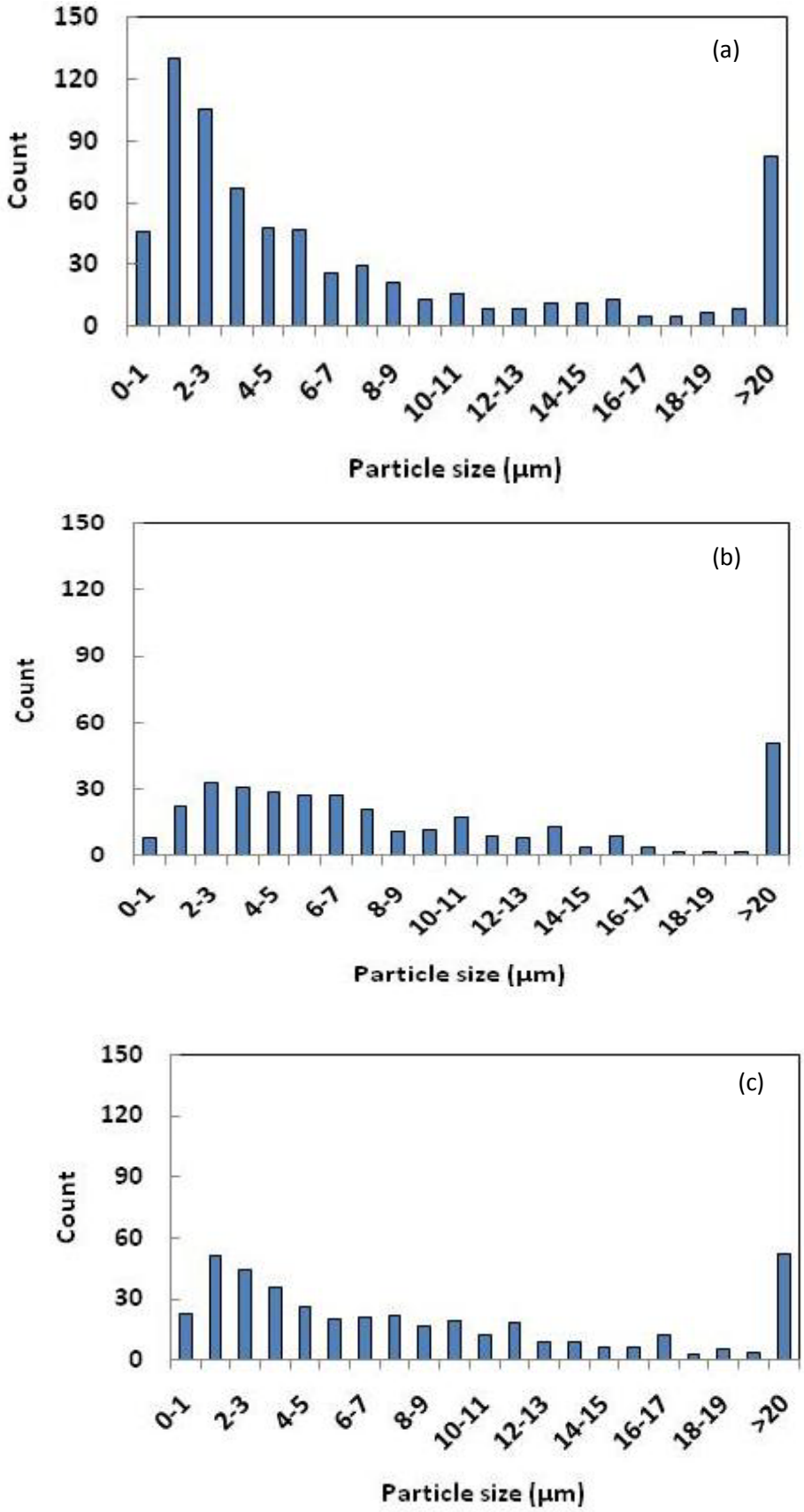

Figure 27. The particle distribution of (a) as-melt-spun (b) 2 and (c) 4 h milling $Sm_{10.5}Co_{89.5}$ melt-spun at 20m/s.

Chapter 5. Conclusions

The roles of alloy composition and initial microstructure on the mechanical milling response of Sm-Co alloys were investigated. Two alloy compositions were investigated: $Sm_{10.5}Co_{89.5}$ and Sm_8Co_{92}. Each alloy was melt spun at two different wheel speeds in order to generate different microstructural scales in the starting materials. Mechanical milling resulted in a refinement in microstructural scale, for both $Sm_{10.5}Co_{89.5}$ and $Sm_8Co_{92,}$ producing ~10 – 20 nm $SmCo_7$ grains. Mechanical milling also resulted in coercivity enhancement for both $Sm_{10.5}Co_{89.5}$ and $Sm_8Co_{92,}$ reaching as high as ~4.6 and 1.7 kOe, respectively. The $Sm_{10.5}Co_{89.5}$ alloys had higher coercivity values overall. This is likely due to the relatively large phase fraction of FCC-Co in the Sm_8Co_{92} alloys. The role of initial microstructure is unclear, as a higher coercivity was observed for $Sm_{10.5}Co_{89.5}$ melt-spun at 20 m/s samples compared to $Sm_{10.5}Co_{89.5}$ melt-spun at 40 m/s samples, while no difference in coercivity was observed in the Sm_8Co_{92} samples melt spun at different wheel speeds

Bibliography

1. **Parker, Rollin J.** *Advances in permanent magnetism.* New York : John Wiley & Sons, 1990. ISBN 0-471-82293-0.

2. *Magnetism in future.* **Coey, J.M.D.** 2001, Journal of Magnetism and Magnetic Materials , pp. 2107-2112.

3. *Recent develompents in hard magnetic bulk materials.* **Fidler, J., et al.** Wien : Institute of physics publishing, 2004, Journal of physics: Condensed matter, Vol. 16, pp. S455-S470.

4. *Nanophase hard magnets.* **Hadjipanayis, George C.** Delaware : Elsevier, 1999, Journal of magnetism and magnetic materials, Vol. 200, pp. 373-391.

5. *Modeling of vial and ball motions for an effective mechanical milling process.* **Budin, Salina, et al.** 2009, Journal of Materials Processing Technology, Vol. 209, pp. 4312-4319.

6. *Mechanically alloyed Sm-Co materials.* **Wecker, J., Katter, M. and Schultz, L.** 8, Erlangen : s.n., April 15, 1991, Journal of Applied Physics, Vol. 69, pp. 6058-6060.

7. *Magnetic properties and microstructure of mechanically milled Sm2(Co,M)17-based powders with M=Zr, Hf, Nb, , Ti, Cr, Cu and Fe.* **Chen, Z., et al.** Newark : s.n., April 1, 200, Journal of applied physics, pp. 3409-3414.

8. *Mechanically alloyed nanocomposite magnets (invited).* **McCormick, P.G., et al.** 11, Nedlands : American institute of physics, June 1, 1998, Journal of applied physics, Vol. 83, pp. 6256-6261.

9. *Rapid Soldificaton of Sm-Co permanent magnets.* **Ravindran, V.K. and Shield, J.E.** Lincoln : Phase Transformations in Magnetic Materials, 2007, Metallurgical and materials transactions A, pp. 732-737.

10. *Phase formation and magnetic properties of SmCo(5+x) alloys with the TbCu7-type structure.* **Aich, S. and Shield, J.E.** Lincoln : Elsevier, 2004, Journal of magnetism and magnetic materials, Vol. 279, pp. 76-81.

11. **Jiles, David.** *Introduction to magnetism and magnetic materials.* 1st Edition. New York : Chapman and Hall, 1991. ISBN 0-412-38630-5.

12. **Callister, William D.** *Materials Science and Engineering.* New York : John Wiley & Sons, 2007. ISBN 0-471-13576-3.

13. **Spaldin, Nicola.** *Magnetic materials: fundementals and device applications.* New York : Cambridge university press, 2003. ISBN 0-521-81631-9.

14. **Rogge, Paul.** *Directional crystallization of melt-spun rare-earth permanent magnets using a temperature gradient heat treatment process.* Mechanical Engineering. Lincoln : University of Nebraska-Lincoln, 2008. A Thesis.

15. **Skomski, Ralph.** *Simple models of magnetism.* Lincoln : Oxford university press, 2008. ISBN 978-0-19-857075-2.

16. **Hopwood, Claire and Brook, David.** Ferromagnetic Materials. *DoITPoMS Teaching and Learning Packages.* [Online] [Cited: October 20, 2009.] http://www.msm.cam.ac.uk/doitpoms/tlplib/ferromagnetic/printall.php.

17. *Nanomagnetics.* **Skomski, R.** R841–R896, Lincoln, NE : Institute of physics publishing, 2003, Journal of Physics: Condensed Matter, Vol. 15.

18. **Gould, J.E.** *Cobalt monograph series: cobalt alloy permanent magnets.* Brussels : Centre D'Information Du Cobalt, 1971.

19. *Nanocomposite Sm2Co17/Co permanent magnets by mechanical alloying.* **Chen, S.K., Tsai, J.L. and Chin, T.S.** 8, Taichung : American Institue of Physics, April 15, 1996, Journal of applied physics, Vol. 79, pp. 5964-5966.

20. *A new class of Sm-TM magnets for operating temperatures up to 550C.* **Walmar, Marlin S., Chen, Christina H. and Walmar, Michael H.** 5, Landisville : s.n., September 2000, IEEE Transactions on magnetics, Vol. 36.

21. **Massalski, T.B., et al.** *Binary alloy phase diagram.* 2nd Edition. Ohio : ASM internaional, 1990. Vol. 2. ISBN 0-87170-405-6.

22. Sigma-Aldrich. [Online] [Cited: March 1, 2010.] http://www.sigmaaldrich.com/materials-science/metal-and-ceramic-science/magnetic-alloys.html.

23. National ImportsTM; Magnetic product division. [Online] [Cited: October 11, 2009.] http://www.rare-earth-magnets.com/magnet_university/types_of_magnets.htm.

24. *Superparamagnetism of Co-Ferrite Nanoparticles.* **Vejpravova, J.P, et al.** Prague : s.n., 2005, Proceedings of Contributed papers, Vol. III, pp. 518-523. ISBN 80-86732-59-2.

25. *Magnetic reversal in three-dimensional exchange-spring permanent magnets.* **Shield, J.E, et al.** 99, Lincoln : American instutite of physics, 2006, Journal of applied physics.

26. *SmCo5/alfa-Fe nanocomposite material obtained by mechanical milling and annealing.* **Pop, V., et al.** 2, Cluj-Napoca : s.n., April 2, 2006, Journal of optoelectronics and advanced materials, Vol. 8, pp. 494-500.

27. *Cluster-assembled exchange-spring nanocomposite permanent magnets.* **Rui, X., et al.** Lincoln : American institute of physics, 2005, Journal of applied physics, Vol. 97, pp. 10K310-1 - 10K310-3.

28. *Rapidly solidified nanocomposite SmCo7/fcc Co permanent magnets.* **Shield, J.E, et al.** Lincoln : Elsevier, 2005, Scripta Maerialia, Vol. 52, pp. 75-788.

29. *A mechanism of magnetic hysteresis in heterogeneous alloys.* **Stoner, E.C and Wohlfarth, E.P.** Leeds : JSTOR, 1947, Philosophical transactions of the Royal Society of London: Series A, Vol. 240, pp. 599-642.

30. **Shield, J.E.** *Unpublished.* Lincoln, Oct 2009.

31. **Kelsell, Robert W., Hamley, Ian W. and Geoghegan, Mark.** *Nanoscale science and technology.* Hoboken : John Wiley & Sons Ltd, 2005. ISBN 0-470-85086-8.

32. **Suryanarayana, C.** *Mechanical alloying and milling.* New York : CRC Press, 2004. ISBN 0-8247-4103-X.

33. **Suryanarayana, C. and Grant Norton, M.** *X-ray diffraction: a practical approach.* 1st Edition. New York : Plenum Press, 1998. ISBN 0-3064-5744-X.

34. *Princeton measurement corporations handbook for the Model 2900 Micromag System.* Princeton : AGFM Handbook, 02/18/92.

35. *An alternating-gradient magnetometer(invited).* **Flanders, P.J.** Philadelphia : s.n., April 15, 1988, Journal of applied physics, Vol. 63, pp. 3940-3945.

36. **Brundle, C. Richard, Evans, Charles A.,Jr and Wilson, Shaun.** *Encyclopedia of Materials characterization.* Greenwich : Manning Publication Co., 1992. ISBN 0-7506-9168-9.

37. Image Processing and Analysis in Java. [Online] http://rsbweb.nih.gov/ij/.

38. **Keeler, Wendy A.** *Eutectic solidification limits and mechanical properties of Sm-Co-Fe alloys.* Mechanical Engineering, University of Nebraska. Lincoln : s.n., 2010. M.S Thesis.

39. *Field-ball milling induced anisotropy in magnetic particles.* **Poudyal, N., et al.** Arlington : IOP Publishing Ltd, December 2, 2004, Journal of Physics D: Applied physics, Vol. 37, pp. L45-L48.

40. *High coercivity in nanostructured PrCo-based powders produced by mechanical milling and subsequent annealing.* **Chen, Z., Meng-Burany, X. and Hadjipanayis, G.C.** 20, Delawere : s.n., November 15, 1999, Applied physics letters, Vol. 75, pp. 3165-3167.

41. *1:7-type magnets produced by mechanical milling.* **Venkatesan, M., Jiang, C. and Coey, J.M.D.** Dublin : Elsevier Science, 2002, Journal of magnetism and magnetic materials, Vols. 242-245, pp. 1350-1352.

42. *Microstructure and magnetic properties of uncoupled Sm2Co17-Cu nanocomposites.* **Zhang, J.X., et al.** 11, Thiais : American institute of physics, March 18, 2002, Applied physics letters, Vol. 80, pp. 1960-1962.

43. *Crystal structure and magnetic performance of single-phase nanocrystalline SmCo7 alloy.* **Zhang, Z.X., et al.** Beijing : Elsevier Ltd., 2010, Scripta materialia, Vol. 62, pp. 594-597.